



A review of recent progress in thermoelectric materials through computational methods

J. Julio Gutiérrez Moreno^{1,2} · Jiang Cao³ · Marco Fronzi⁴ · M. Hussein N. Assadi⁵

Received: 28 February 2020 / Accepted: 26 June 2020
© The Author(s) 2020

Abstract

Reducing our overwhelming dependence on fossil fuels requires groundbreaking innovations in increasing our efficiency in energy consumption for current technologies and moving towards renewable energy sources. Thermoelectric materials can help in achieving both goals. Moreover, because of recent advances in high-performance computing, researchers more increasingly rely on computational methods in discovering new thermoelectric materials with economically feasible performance. In this article, significant thermoelectric materials discovered through these computational methods are systematically reviewed. Furthermore, the primary computational tools that aid the design of the next-generation thermoelectric materials are introduced and discussed. These techniques include various levels of density functional theory, electronic transport simulations, and phonon calculations.

Keywords Thermoelectric materials · Heterostructures · Density functional theory · DFT + U · Transport phenomena · Phonon dispersion

List of symbols

AIMD	Ab initio molecular dynamics
DFPT	Density functional perturbation theory
DFT	Density functional theory
DFTB	Density functional tight-binding
DOS	Density of states
E	Electric field
E_F	Fermi level
EMC	Ensemble Monte Carlo

f	Energy function
g	Degeneracy
GGA	General gradient approximation
GW	Self-energy correction approximation
IFC	Interatomic force constant
IoT	Internet of Things
j	Current density
J	Exchange term
\mathbf{k}	Momentum vector
K	Kelvin
k_B	Boltzmann constant
L	Lorenz number
LDA	Local density approximation
MD	Molecular dynamics
n	Carrier concentration
N_D	Concentration of donor atoms
n_{ref}	Reference carrier concentration
P	Pressure
PBTE	Peierls–Boltzmann transport equation
PDOS	Partial density of states
PGEC	Phonon-glass electron-crystal
R_c	Critical distance
S	Entropy
S_{Coeff}	Seebeck coefficient
$S_{\text{Coeff}}^{\text{Max}}$	Maximum Seebeck coefficient

✉ Jiang Cao
jiang.cao@njust.edu.cn

✉ M. Hussein N. Assadi
h.assadi.2008@ieee.org

¹ Department of Computer Applications in Science and Engineering, Barcelona Supercomputing Center (BSC), C/ Jordi Girona 29, 08034 Barcelona, Spain

² Institute for Advanced Study, Shenzhen University, Shenzhen 518060, China

³ School of Electronic and Optical Engineering, Nanjing University of Science and Technology, Nanjing 210094, China

⁴ School of Mathematical and Physical Science, University of Technology Sydney, Sydney, NSW 2007, Australia

⁵ School of Materials Science and Engineering, University of New South Wales, Sydney, NSW 2052, Australia

SSCHA	Stochastic self-consistent harmonic approximation
T	Temperature
T_C	Temperature of cold reservoir
TE	Thermoelectric
T_H	Temperature of hot reservoir
t_1	Hopping integrals
T_M	The average of T_C and T_H
u	Infinitesimal displacement
U	Hubbard term
U_{eff}	Effective Hubbard term
v	Group velocity
V	Potential
V	Volt
VCA	Virtual crystal approximation
ZT	Figure of merit
α_κ	First power factor for thermal conductivity
β_κ	Second power factor for thermal conductivity
ε	Quasiparticle energy/band energy
η	Efficiency
κ	Thermal conductivity
κ_{300}	Thermal conductivity at 300 K
κ_e	Electronic part of thermal conduction
κ_L	Lattice part of thermal conduction
μ	Chemical potential
μ	Micro
μ_e	Electron mobility
N	Thermoelectric conductivity
ρ	Electrical resistivity
σ	Electrical conductivity
Ω	Unit cell volume

Introduction

More than 70% of the global energy consumption is lost during conversion as waste heat [1], released to the environment at a wide range of temperatures (300–1000 K). This wasted energy originates from numerous sources such as mining and smelting plants, factories, electricity generators, air-conditioning and lighting appliances, pipelines, vehicles' engines, brakes and exhausts, and even the human body. Harvesting this waste heat is of paramount importance for improving energy consumption efficiency. One promising solution is the thermoelectric (TE) effect [2], which governs the direct conversion of heat to electricity in a TE material. Additionally, TE materials can further reduce the CO₂ emissions, and enable extensive deployment of battery- and grid-free devices, wearable electronics, the Internet of Things (IoT), and much more. The performance of a thermoelectric material at a given temperature T is quantified by its figure of merit (ZT). ZT is defined as $ZT = S_{\text{Coeff}}^2 \sigma T / \kappa$, where S_{Coeff} is the Seebeck coefficient, σ is the electrical conductivity, and κ

is the thermal conductivity. κ is made of two contributions: the electronic thermal conductivity (κ_e) and the lattice or phonon thermal conductivity (κ_L). Maximizing ZT in thermoelectric materials requires three criteria satisfied: first, a large S_{Coeff} , to obtain the highest electric potential difference for a given temperature gradient; second, a low κ , to delay the thermal equilibration between the heat source and the environment; last, a high σ , to generate the highest current for the thermo-voltage.

To construct a TE harvesting unit, one must interface an n -type TE material to a p -type TE material, forming an n - p TE junction. Then, by putting one side of the TE junction in contact with a hot surface (waste heat source) and the other side with a cold surface (ambient), electricity is generated on the cold side. Several couples of the TE junctions are usually coupled together, both serially and in parallel, forming a TE module, shown in Fig. 1, to increase the amount of harvested energy. Such a configuration is commonly achieved by cutting n - and p -type bars from sintered pellets [3], or preparing n - and p -type thin films epitaxially deposited on an inflexible single-crystal substrate [4]. The primary appeal of TE generators is the fact that they are capable of converting waste heat directly into electrical energy without any moving parts. As a result, research thrived and plenty of TE materials (alloys, oxides, and nitrides) were discovered. After nearly a century of research and development, however, the practical use of TE devices is still limited to

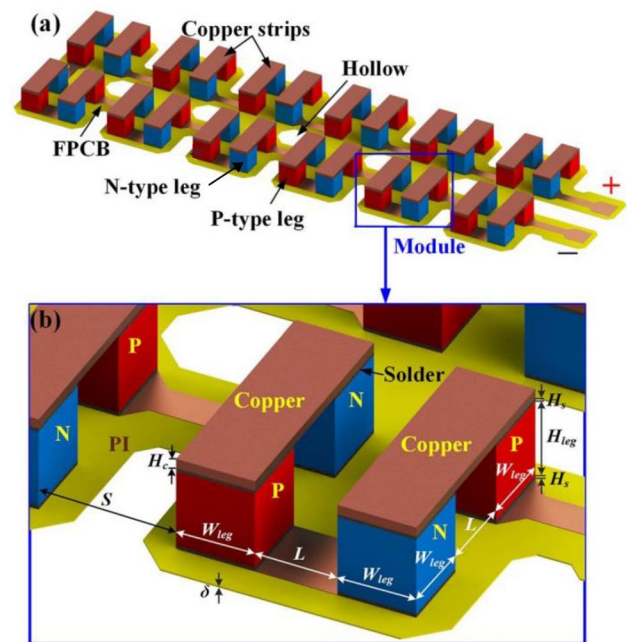


Fig. 1 Structural design of wearable thermoelectric harvesting device: **a** schematic view; **b** close-up view of one thermoelectric module. Adapted with permission from Ref.[12]. Copyright 2018 IEEE

niche applications [5–7]. There are three significant obstacles against the widespread application of TE harvesters: (i) the low conversion efficiency and low chemical stability of TE materials; (ii) the toxicity and criticality of elements used in TE materials; and (iii) the mechanical rigidity of TE modules that impedes application in wearables.

In the search for high-performance thermoelectric materials, it has now become evident that the traditional materials' engineering approach based on judicious choice of materials and synthesis conditions via trial-and-error would only result in little improvement of the TE performance [8, 9]. As a result, a theory-guided approach in the search for suitable high-performance thermoelectric materials with favorable electronic and thermal transport is becoming common [10–12]. In this review, we, therefore, systematically examine and present the recent developments in thermoelectric research propelled by theoretical and computational methods. The theoretical tools reviewed here can be divided into two broad categories: (a) electronic-structure calculations and that deal with S , σ , and κ_e ; and (b) lattice dynamics or phonon calculations that determine κ_L . Although these two types of calculations are interrelated, they, nonetheless, describe fundamentally different aspects of the materials' properties. As such, different computational tools have been developed for electronic and lattice dynamics calculations, of which both are covered here.

The need for computational insight

The second law of thermodynamics fundamentally dictates the upper limit efficiency of any thermodynamic engine, including the thermoelectric power generators. The efficiency (η) of a solid-state power generator, as a function of ZT , operating between hot and cold reservoirs with temperatures T_H and T_C is given by the following nonlinear expression [13]:

$$\eta = \frac{T_H - T_C}{T_H} \left[\frac{(1 + ZT_M)^{1/2} - 1}{(1 + ZT_M)^{1/2} + (T_C/T_H)} \right], \quad T_M = (T_H + T_C)/2. \quad (1)$$

The challenge in achieving high ZT ($S_{\text{Coeff}}^2 \sigma T / \kappa$) materials lies in the interdependency of the κ , σ , and S_{Coeff} in any given material system, as all are functions of the carrier concentration (n). For instance, in an isotropic n -type semiconductor, σ can be expressed as:

$$\sigma(T, n) = e \cdot n(T) \cdot \mu_e(T, n), \quad (2)$$

in which e is the unit charge and $\mu_e(T, n)$ is the electron mobility. $\mu_e(T, n)$ is governed by a multitude of scattering mechanisms that often vary with T and carrier concentration, in a complex manner. $n(T)$, in turn, is commonly controlled

by extrinsic doping. S_{Coeff} can be generally expressed by the formula [14]:

$$S_{\text{Coeff}}(T, n) = -\frac{k_B}{e} \cdot \left(\frac{5}{2} - \ln \frac{n(T)}{N_D} \right), \quad (3)$$

in which k_B is the Boltzmann constant, and N_D is the concentration of n -type (donor) dopants. One should note that Eq. 3 only holds at relatively large $n(T)$ as S_{Coeff} diverges when $n(T)$ approaches zero [15]. As can be easily deciphered, σ in thermoelectric semiconductors can be raised by carrier doping. As an undesired side effect, however, the additional carriers decrease S_{Coeff} , resulting in a meager or no net benefit to the ZT .

Furthermore, the relation between κ and n is even more complicated. κ_e is related to σ by the Wiedemann–Franz law [16]. As a result, any carrier doping unfavorably boosts the electronic share of the thermal conductivity, while κ_L , which is the dominant thermal conduction mechanism over a wide range of carrier concentrations in semiconductors, depends on the density, heat capacity, and thermal diffusivity of which all are influenced by doping. For all these complications, κ is often phenomenologically modeled as a temperature- and concentration-dependent power law [17]:

$$\kappa = \kappa_{300} \left(\frac{T}{300 \text{ K}} \right)^{\sigma_\kappa} \cdot \left(1 + \left(\frac{n(T)}{n_{\text{ref}}} \right)^{\beta_\kappa} \right). \quad (4)$$

Here, κ_{300} is the thermal conductivity at 300 K, while n_{ref} , σ_κ , and β_κ are constants to be determined by fitting experimental measurements. In the intrinsic range, both electrons and holes contribute toward κ , constituting a bipolar contribution towards κ . The heavier an n -type semiconductor is doped, however, the more generous the κ_e contribution is towards κ .

A reflection upon the complex interdependence of S_{Coeff} , σ , and κ , one recognizes the challenges of designing high-efficiency thermoelectric materials. The challenges arising from carrier doping are schematically presented in Fig. 2. In addition to the electronic requirements, one must also consider other constraints such as the non-toxicity and the abundance of the elements used (usually associated with the price and sustainability), mechanical robustness, moist resistance, flexibility (for wearables), and the low dopant solubility in some cases, to mention a few. As a result, the typical experimental approach in finding new thermoelectric materials inspired by search within a composition or structural space similar to known materials is very restrictive by nature. Consequently, by resorting to computationally guided materials search, design, and discovery, one may accelerate the pace of the progress in TE research beyond the limit imposed by the judicious and serendipitous experiments.

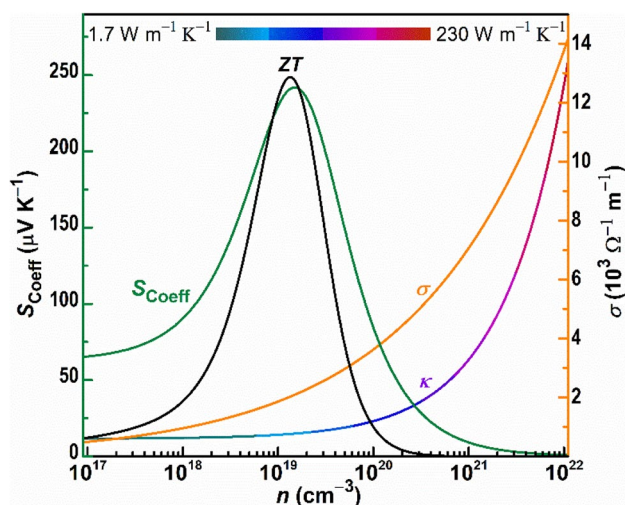


Fig. 2 The dependence of S_{Coeff} , σ , and κ on carrier concentration (n) for polycrystalline $\text{Pb}_{1-x}\text{Sn}_x\text{Te}$ at 300 K. ZT reaches its maximum only for a very narrow window of n . A change in temperature shifts all these curves in a non-trivial manner, resulting in a maximum ZT at a different n . Furthermore, synthesis protocols may drastically change the presented values. S_{Coeff} and σ values were adapted from Refs. [18] and [19], while κ was adapted from Ref. [20]

Electronic calculations

The electronic description

The efficiency of the thermoelectric energy conversion is directly related to the materials' non-dimensional figure of merit, which grows linearly with the electrical conductivity [21]. The essential quantities are then σ , together with the S_{Coeff} , which are determined by the electronic structures of the materials and by carrier-scattering processes. Currently, there are two main approaches for calculating the electron transport properties and S_{Coeff} : the semiclassical formulas based on Boltzmann transport theory; and the fully quantum-mechanical approach described in the Kubo–Greenwood theory [22–24]. An alternative, fully quantum-mechanical approach has also been developed by Landauer [25]. Here, the scattering processes are modeled as if they build charges and fields inside the materials, which represents an alternative view to that of Kubo's method in which currents are formed in response to a given external electric field. The Landauer methodology intimately resembles the experimental viewpoint, where one usually imposes an external current and measures the resulting potential drop due to the electron scattering, which is an important tool in guiding intuition when studying mesoscopic transport properties.

The semiclassical Boltzmann transport equation, however, has gained appreciable popularity in recent years due

to the ease of use and its integration with a diverse range of density functional theory (DFT) codes. The semiclassical Boltzmann transport equation, as implemented in the prominent BoltzTrap [24] and BoltzTrap2 [26] packages, relies only on the DFT calculated band and \mathbf{k} -dependent quasiparticle energies (ϵ) as input. It then extrapolates the transport properties within the rigid band approximation [24]. Furthermore, this method assumes a T and ϵ independent relaxation time (τ) for electronic scatterings which results in a tractable and straightforward form of the equations for S_{Coeff} , σ , and κ_e . The constant relaxation-time approximation, despite its simplicity, predicts S_{Coeff} values that match well with experiments and is widely adopted in the high-throughput theoretical search of novel TE materials. Table 1 summarizes some of the recent predictions using the BoltzTrap package.

In brief, the Boltzmann transport equation describes the general statistical behavior of a system out of thermodynamic equilibrium in terms of local equilibrium distributions. The Boltzmann transport equation is derived by assuming random motion of particles—in this case, electrons—within a medium, leading to the formulation of a current (j) in terms of conductivity tensors:

$$j_i = \sigma_{ij}E_j + N_{ij}\nabla_j T, \quad (5)$$

in which σ_{ij} and N_{ij} are the elements of the electrical and thermoelectric conductivity tensors. From the band structure, within the rigid band approximation, the conductivity tensors along the reciprocal lattice direction α and β can be obtained as follows:

$$\sigma_{\alpha\beta}(i, \mathbf{k}) = e^2 \tau_{i,\mathbf{k}} v_{\alpha}(i, \mathbf{k}) v_{\beta}(i, \mathbf{k}), \quad (6)$$

where e is the electron charge, $\tau_{i,\mathbf{k}}$ is the relaxation time, $v(i, \mathbf{k})$ is the group velocity, i is the band index, and \mathbf{k} is the reciprocal (crystal momentum) vector. Here, $v(i, \mathbf{k})$ can be calculated from the band structure by taking the derivative of the band energy function (f) over \mathbf{k} . Here, the relaxation time ($T_{i,\mathbf{k}}$) describes how quickly the system returns to thermodynamic equilibrium after scattering events. $T_{i,\mathbf{k}}$ plays an important role in determining the transport properties such as electron mobility, electrical conductivity, thermal conductivity, and Seebeck coefficient. $T_{i,\mathbf{k}}$ principally depends on both the band index (i) and the \mathbf{k} vector direction. However, several studies of the direction dependence have shown that $T_{i,\mathbf{k}}$ can be considered, with a good approximation, direction-independent in almost all known crystals [27]. A further approximation of $T_{i,\mathbf{k}}$ to a constant value leads to an expression for the Seebeck coefficient that is also independent of the relaxation time. However, an important restriction for the relaxation-time approximation to be valid is that the time the distribution function takes to relax to its equilibrium is independent of the distribution function itself and the externally

applied electric field. By integrating $\sigma_{\alpha\beta}$ over the energy (ϵ) space, the transport tensor can be obtained as:

$$\sigma_{\alpha\beta}(T, \mu) = \frac{1}{\Omega} \int \sigma_{\alpha\beta}(\epsilon) \left[-\frac{\partial f_{\mu}(T, \epsilon)}{\partial \epsilon} \right] d\epsilon, \quad (7)$$

$$N_{\alpha\beta}(T, \mu) = \frac{1}{eT\Omega} \int \sigma_{\alpha\beta}(\epsilon - \mu) \left[-\frac{\partial f_{\mu}(T, \epsilon)}{\partial \epsilon} \right] d\epsilon, \quad (8)$$

$$\kappa_{\alpha\beta}(T, \mu) = \frac{1}{e^2 T \Omega} \int \sigma_{\alpha\beta}(\epsilon - \mu)^2 \left[-\frac{\partial f_{\mu}(T, \epsilon)}{\partial \epsilon} \right] d\epsilon, \quad (9)$$

in which μ is the electronic chemical potential, and Ω is the unit cell volume. Finally, the Seebeck coefficient can be easily computed as follows:

$$S_{ij} = (\sigma^{-1})_{ai} N_{aj}. \quad (10)$$

The physical limitation to the semiclassical Boltzmann theory is that it is only valid for the first-order terms, while it more or less fails at higher orders. This shortcoming is due to the assumption of chaotic molecular motion in Boltzmann's

collision integral—an approximation that is only accurate up to first order [28]. However, the equivalence of the two most critical theoretical methods for the calculation of electronic transport within the linear regime has been explicitly demonstrated, and both of them allow the calculation of electric transport and S_{Coeff} from first-principles (ab initio) calculations, namely DFT. The excellent agreement between the calculated results and the experimental data reported in the literature validates the validity of the transport theories when coupled with ab initio computational methods [29–31].

Wannier functions

The maximally localized Wannier function representation allows us to naturally introduce the ground-state electronic structure into the lattice Green's function approach that will be the basis for the evaluation of the Landauer quantum conductance [42, 43]. This approach is computationally efficient, can be easily implemented as a postprocessing step in standard electronic-structure DFT calculations, and allows us to link the electronic transport properties of a device to the nature of the chemical bonds directly, providing an

Table 1 The predicted S_{Coeff} values for the TE materials, calculated with the BoltzTrap package that have recently reported in the literature

Compound	Structure	S_{Coeff} ($\mu\text{V K}^{-1}$)	T (K)	Notes	References
CoFeMnSb	Quaternary Heusler	~800	300	S_{Coeff} monotonically falls with rising T	[32]
SbSeI	Half-Heusler	~380	300	S_{Coeff} monotonically falls with rising T . $S_{\text{Coeff}}^{\text{max}} = 850 \mu\text{V K}^{-1}$ at 100 K	[33]
SbSI	Half-Heusler	~210	300	S_{Coeff} is approximately constant for $300 \text{ K} < T < 800 \text{ K}$	[33]
SbSBr	Half-Heusler	~200	300	S_{Coeff} is approximately constant for $300 \text{ K} < T < 800 \text{ K}$	[33]
TiSiSb	Half-Heusler	~204	300	S_{Coeff} pertains to S_{xx} direction and majority carriers, negligible for any other case	[34]
TiGeSb	Half-Heusler	~140	300	S_{Coeff} pertains to S_{xx} direction and majority carriers, negligible for any other case	[34]
CdCr ₂ O ₄	Spinel	~215	300	S_{Coeff} falls monotonically with rising T . $S_{\text{Coeff}}^{\text{max}} = 220 \mu\text{V K}^{-1}$ at $T = 200 \text{ K}$	[35]
ZnCr ₂ O ₄	Spinel	~210	300	S_{Coeff} falls monotonically with rising T . $S_{\text{Coeff}}^{\text{max}} = 218 \mu\text{V K}^{-1}$ at $T = 200 \text{ K}$	[35]
CdV ₂ O ₄	Spinel	~45	800	S_{Coeff} monotonically increases with rising T up to 800 K	[36]
HgV ₂ O ₄	Spinel	~30	800	S_{Coeff} monotonically increases with rising T up to 800 K	[36]
ZnV ₂ O ₄	Spinel	~15	300	S_{Coeff} monotonically falls with rising T . $S_{\text{Coeff}}^{\text{max}} = \sim 22 \mu\text{V K}^{-1}$ at $T = 200 \text{ K}$	[36]
Sr ₂ MnTaO ₆	Double Perovskite	~130	400	S_{Coeff} is a concave function of T and peaks at $T = 400 \text{ K}$	[37]
PdTiO ₃	Perovskite	~145	800	S_{Coeff} monotonically increases with rising T up to 800 K	[38]
SnTiO ₃	Perovskite	~135	800	S_{Coeff} monotonically increases with rising T up to 800 K	[38]
CaCrO ₃	Perovskite	~73	800	S_{Coeff} monotonically increases with rising T up to 800 K	[39]
SrCrO ₃	Perovskite	~64	800	S_{Coeff} monotonically increases with rising T up to 800 K	[39]
BaCrO ₃	Perovskite	~40	800	S_{Coeff} monotonically increases with rising T up to 800 K	[39]
SrTi _{0.92} Ho _{0.08} O ₃	Doped Perovskite	~74	550	S_{Coeff} is a concave function of T and peaks at $T = 550 \text{ K}$	[40]
SrTi _{0.92} Ta _{0.08} O ₃	Doped Perovskite	~69	800	S_{Coeff} monotonically increases with rising T up to 800 K	[40]
La _{0.82} Ba _{0.18} CoO ₃	Doped Perovskite	~15	300	S_{Coeff} is maximum at $T = 300 \text{ K}$, S_{Coeff} is a convex function of T	[41]

The S_{Coeff} were reported for temperatures at which S_{Coeff} was either maximum ($S_{\text{Coeff}}^{\text{max}}$) or for 300 K if S_{Coeff} peaked below room temperature

insight into the mechanisms that govern electron flow at the nanoscale. Owing to the exponential localization of the Wannier functions obtained from plane waves, accurate integrations over the Brillouin zone can be achieved at a very moderate computational cost. Moreover, the analytical expression for the band derivatives in the Wannier basis resolves any issues that may occur when evaluating derivatives near band crossings. The accuracy of the results on a coarse \mathbf{k} -point reciprocal-space grid using Wannier functions was confirmed by Pizzi et al., who performed calculations of the electrical conductivity on the binary and ternary skutterudites CoSb_3 and $\text{CoGe}_{3/2}\text{S}_{3/2}$ [44]. Moreover, the semiclassical Boltzmann transport theory based on maximally localized Wannier functions with constant relaxation-time approximation was applied to examine the transport properties of SrTiO_3 [45]. The results for the transport properties show the prospect of thermoelectric presentation for SrTiO_3 at different temperatures from 300 to 800 K as a function of chemical potential, which plays an important role. Varying the temperature in terms of chemical potential shows a remarkable enhancement in the TE performance for the properties of thermoelectric materials. In the considered cubic phase, the chemical potential of SrTiO_3 is equal to the sum of all atomic component chemical potentials in the crystal [45].

In search of flat bands

The band dispersion, in other words, the slope of the bands near band edges, is of great importance for predicting materials' TE performance. Steeper slopes indicate stronger orbital interactions and faster carrier mobility. On one hand, for stronger orbital interactions, the band becomes more disperse in energy. On the other hand, weaker orbital interactions correspond to flatter bands. This simple model elucidates the fact that dispersed bands lead to higher carrier mobility, while flat bands indicate more localized carriers. However, there is a class of fermion systems with a diverging density of states (DOS). These type of materials, such as CuAlO_2 [46], exhibit a dispersionless spectrum that have precisely zero dispersion, the so-called flat band [47]. Flat bands can emerge in strongly interacting condensed matter systems and layered compounds with integer-valued pseudo-spin [48–52].

Ishii et al. found that the electric current flowing along the chain suddenly increases the magnitude when a minimal electric field is applied to the system. This large current originates from the symmetry breaking of the large energy degeneracy of flat-band states in the Kagome lattice, which is nearly independent of the size of the Kagome-lattice chain itself [53]. Under flat-band conditions, Ishii et al. showed that carriers in high-lying minibands could propagate for several superlattice periods without being scattered. These carriers follow the

miniband description of transport. In a uniform electric field, the minibands break down into localized states immediately. These states participate in conduction. One strategy to achieve large S_{Coeff} and large electron transport is via low-energy electronic bands containing both, flat and dispersive parts, in different regions of crystal momentum space. This approach is known as the pudding-mold band structure, of which examples are shown in FIG. 3 [54, 55].

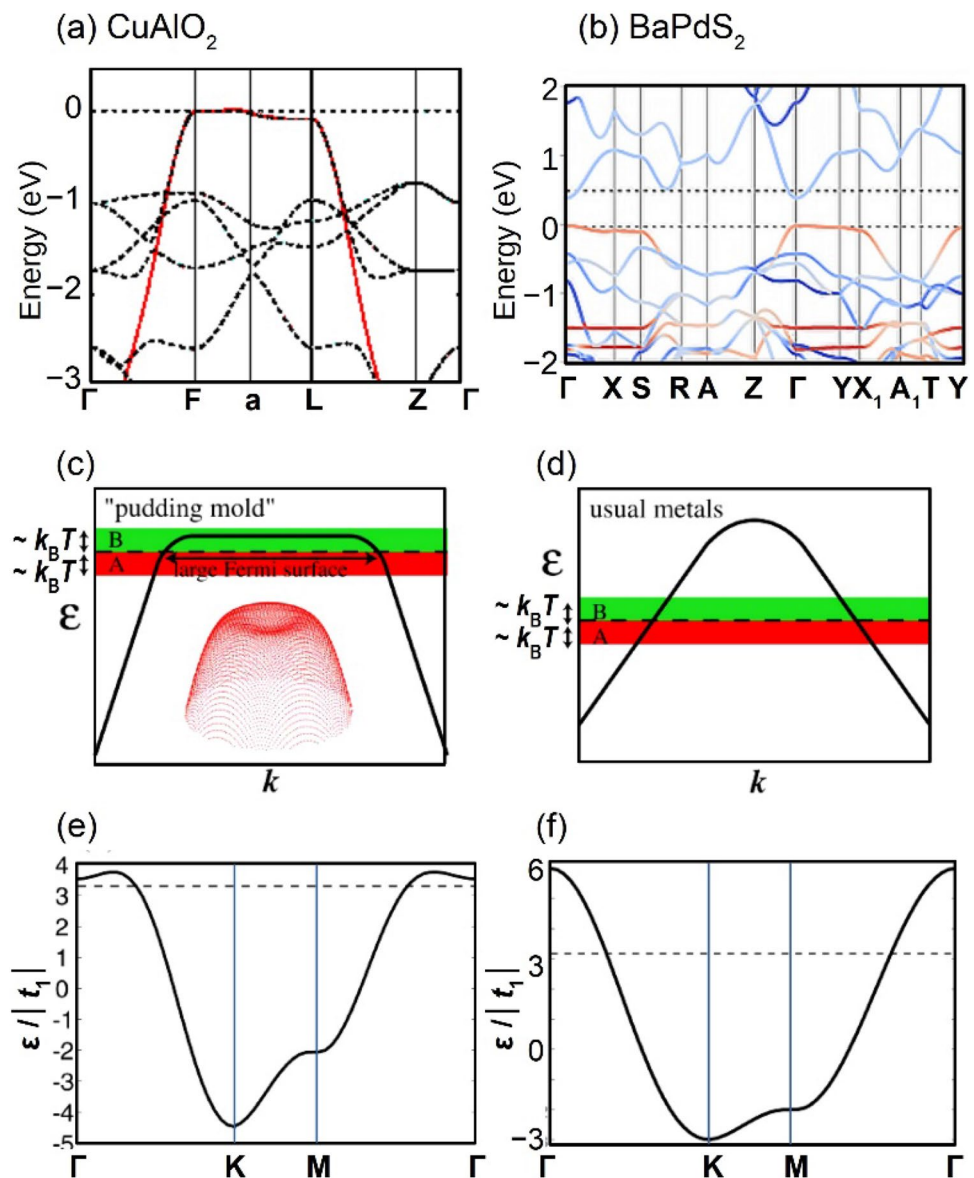
When we consider the problem of electron transport from a more general viewpoint, the literature suggests that most layered compounds are particularly interesting because of their unusual electronic and physical properties, in addition to their desirable thermoelectric performance [56]. For example, through electronic-structure calculations using DFT, a large and anomalous anisotropic thermoelectric transport properties were predicted in d^0 -electron layered complex nitrides AMN_2 (where A and M are metal cations). Subsequently, it was proposed that these compounds may constitute a novel and promising class of TE materials [57–60]. On one hand, because of the dimensionality of the electronic structures, anisotropic electronic transport properties have also been observed in layered oxides $\text{La}_x\text{Sr}_{1-x}\text{CuO}_4$ and Sr_2RuO_4 [61–63]. On the other hand, complex layered nitrides in the form AMN_2 (A = Sr or Na; M = Zr, Hf, Nb, Ta), were analyzed. The Sr containing compounds SrZrN_2 and SrHfN_2 were found to have three-dimensional electronic structures and isotropic thermoelectric transport properties, despite their α - NaFeO_2 -type layered crystal structure [64]. This apparent contradiction can be explained by the fact that the bottom of the conduction bands in these compounds is composed of $\text{Zr } 4d_{z^2} + 4d_{xz} + 4d_{yz}$ and $\text{Hf } 5d_{z^2} + 5d_{xz} + 5d_{yz}$, along with $\text{Sr } 4d_{x^2-y^2} + 4d_{xy}$ orbitals. Here, the A and M ions jointly provide a full set of the d orbitals. However, although the electronic structures of NaNbN_2 and NaTaN_2 are also three-dimensional, NaNbN_2 and NaTaN_2 were found to have weak anisotropic thermoelectric transport properties. This weak anisotropy arises from the NbN_2 and TaN_2 layers whose conduction band minimums are composed of $\text{Nb } 4d_{z^2} + 4d_{xz} + 4d_{yz}$ and $\text{Ta } 5d_{z^2} + 5d_{xz} + 5d_{yz}$ along with $\text{N } 2p_z$ orbitals with no contribution from the Na orbitals. Understanding and elucidating the origin of anisotropic transport properties in layered compounds are of great significance for cultivating this new class of TE compounds, not only for thermoelectric materials but also for realizing novel physical properties [65].

Strongly correlated thermoelectric materials

Spin-driven Seebeck effect

Most conventional thermoelectric materials, of which we reviewed some in the previous section, are semiconductors,

Fig. 3 The red curves in **a, b** show pudding-mold band structure in CuAlO_2 [46] and BaPdS_2 [54], respectively. Schematic figure of the electronic structure within the pudding-mold structure shown in **(c)** and compare to the one of a typical metal **(d)**. Moreover, **e, f** represent the band dispersion [55]. Here, t_1 is the hopping integral between neighboring sites, and ε is the quasiparticle energy. The dotted gray lines mark the position of the chemical potential for a given temperature T . Adapted with permission from Refs. [46, 54, 55]. Copyrights 2013, and 2019 American Physical Society and 2007 Physical Society of Japan



rather than metals, and, consequently, have low intrinsic electrical conductivity. That is because although metals are the ideal conductors, they, nonetheless, have a diminishingly small S_{Coeff} . The carrier symmetry at the Fermi level (E_F) can explain metals' small Seebeck coefficient, as it implies the number of hot electrons above E_F and cold empty states below E_F are roughly equal. When the number of diffused holes and electrons under a temperature difference is roughly the same, the net Seebeck effect is minimal due to cancellation. Semiconductors circumvent this problem by having only one type of majority carriers. There is, however, one class of thermoelectric materials that noticeably deviates from the conventional paradigm, i.e., the strongly correlated thermoelectrics. Thermoelectric materials such as $\text{Ca}_3\text{Co}_4\text{O}_{9+\delta}$ [66], $\text{Fe}_{1+y}\text{Te}_{0.6}\text{Se}_{0.4}$ [67], and Na_xCoO_2 [68] are excellent

electrical conductors— Na_xCoO_2 has a high carrier concentrations (n) which is in the order of $\sim 10^{21}$ to 10^{22} cm^{-3} [69]. In these materials, spin entropy flow drives the Seebeck effect. For instance, in Na_xCoO_2 , the susceptible spin population is approximately equal to the hole population and remains constant with decreasing T . Na_xCoO_2 , therefore, has a conductivity similar to a metal and a magnetic behavior similar to a frustrated insulator. Such compounds are known as Curie–Weiss metals [70, 71]. Wang et al. [72] demonstrated that at $T=2 \text{ K}$, a magnetic field completely suppresses S_{Coeff} to nil. The disappearance of S_{Coeff} in Na_xCoO_2 , when an external magnetic field aligns all the spins, implies that the Seebeck effect originates from the spin entropy flow carried by the holes in the Curie–Weiss phase. In this section, therefore, we review the structural and electronic characteristics of Na_xCoO_2 —the most

investigated such compound—as a representative of the strongly correlated thermoelectric material.

Na_xCoO_2

Sodium cobaltate (Na_xCoO_2) is a strongly correlated oxide [73, 74] with a fairly high thermoelectric figure of merit (ZT) at temperatures around 800 K for $x > 0.5$ [75]. As shown in Fig. 4, the Na_xCoO_2 lattice is made of alternating Na and edge-sharing CoO_2 octahedral layers stacked along the c direction constituting a quasi-two-dimensional system. In Na deficient ($x < 1$) Na_xCoO_2 , each Na vacancy creates a hole converting a Co^{3+} ion into Co^{4+} . As a result, Na_xCoO_2 exhibits p -type conductivity with n inversely proportional to x . Moreover, the coexistence of Co^{3+} and Co^{4+} ions, or charge disproportionation, in the CoO_2 layers generates a competitive Seebeck potential through spin entropy flow [68, 72]. Furthermore, the mobile Na^+ ions diffusively scatter the phonons [70, 76], decreasing κ_L to $\sim 0.01 \text{ W cm}^{-1} \text{ K}^{-1}$ at $\sim 1000 \text{ K}$ [77]—this κ_L value is ~ 100 times smaller than that of ZnO at the same temperature [78].

The electrical transport properties of Na_xCoO_2 have also been reported for different concentrations of Na in several experimental studies [70, 79, 80]; however, the results are

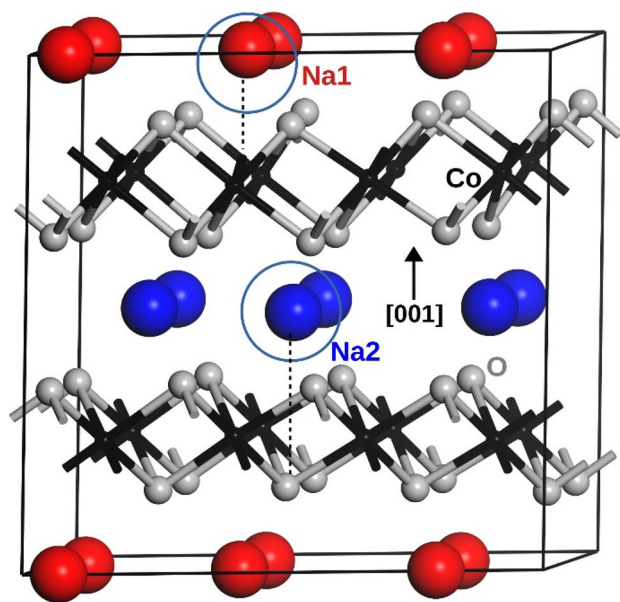


Fig. 4 A schematic presentation of the $\text{Na}_{0.75}\text{CoO}_2$ structure constructed out of a desodiated $4a \times 2a \times 1c$ supercell of the $P6_3/mmc$ Na_1CoO_2 primitive cell. Co and O ions occupy the Wyckoff 2a and 4f sites of the hexagonal lattice structure, respectively. In Na_xCoO_2 , some of the Na ions occupy 2b (Na1) sites which share basal coordinates with Co, while the rest of of the Na ions occupy 2c (Na2) sites which share basal coordinates with O. There are two layers of Na ions (and two layers of CoO_2) in the unit cell. Na ions at $Z=0$ are presented in red, while Na ions at $Z=0.5$ are presented in blue

inconsistent at times and even contradictory. For example, Kawata et al. [79] found that for $x > 0.55$, the electrical resistivity (ρ) of Na_xCoO_2 increases along with increasing x . Motohashi et al. [80], however, found the opposite trend for ρ as a function of x . More recently, Foo et al. used the chemical de-intercalation from $\text{Na}_{0.77}\text{CoO}_2$ to change the Na concentration and found a metal–insulator transition of the charge ordering in $\text{Na}_{0.5}\text{CoO}_2$ single crystal. A similar effect, however, could not be detected in the polycrystalline Na_xCoO_2 prepared by solid-state reaction. In another work, Cui et al. [81] reported a comprehensive study of the structure and electrical transport properties of Na_xCoO_2 ($x = 0.52, 0.56, 0.60, 0.68, 0.72, 0.76, 0.8$). Here, all the samples had metallic conduction, with ρ reaching a minimum at around $x = 0.64$. Moreover, a jump in $\partial\rho/\partial T$ was observed at the temperature corresponding to the dimensional crossover of the electronic transport properties. Some of the discrepancies can be explained by the structural differences between Na_xCoO_2 prepared by solid-state reaction and by chemical de-intercalation from $\text{Na}_{0.77}\text{CoO}_2$. For instance, it was shown that the distance between Co in the CoO_2 layers, which may depend on the synthesis protocol, is critical in determining the electrical transport property of Na_xCoO_2 —and more generally, of all the Na_xTMO_2 (TM = Cr, Mn, Fe, Co, Ni)—where this critical distance R_c that determines whether the compound is insulating or metallic [82]. As seen here, the origin of this difference in observations is still an open question [83, 84] and sets a challenge for theoretical analysis.

Spin entropy flow

The high-temperature S_{Coeff} in Na_xCoO_2 can be expressed by Koshibae’s equation [85, 86] for strongly correlated materials, which itself is a modified form of Heikes formula [87, 88]:

$$S_{\text{Coeff}}(T \rightarrow \infty) = -\frac{k_B}{e} \ln \left[\frac{g(\text{Co}^{3+})}{g(\text{Co}^{4+})} \frac{x}{1-x} \right]. \quad (11)$$

Here, g refers to the degeneracy of the electronic configuration in ions A and B (here $A = \text{Co}^{3+}$ and $B = \text{Co}^{4+}$), and it is equal to all the distinct possible ways which the electrons can be arranged in the orbitals of the ions they occupy. x is the ratio of Co^{4+} over all Co ions, which is proportional to the carrier (hole) concentration, and finally, k_B and e are the Boltzmann’s constant and the electron’s charge, respectively. This concept is schematically demonstrated in Fig. 5. In Na_xCoO_2 , the six electrons of the low-spin Co^{3+} have a $t_{2g}^6 e_g^0$ configuration for which there is no other degenerate state that is entropy $S = \ln[g(\text{Co}^{3+})] = \ln 1$. In contrast, for the low-spin Co^{4+} ion, since one electron is removed, there are six degenerate configurations. Consequently, $S = \ln[g(\text{Co}^{4+})] = \ln 6$. As an electron hops from a Co^{3+} ion

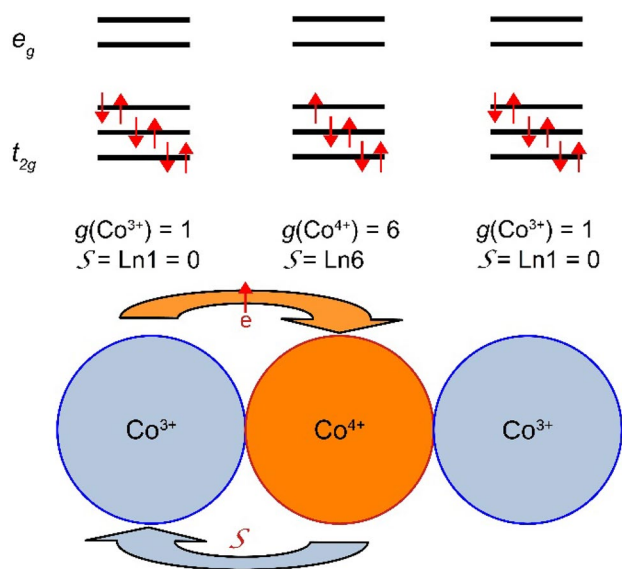


Fig. 5 The schematics of spin entropy flow in Na_xCoO_2 . S and g are the entropy and the electronic degeneracy per site, respectively. Reproduced with permission from Ref. [91]. Copyright 2020 Institute of Physics

to a Co^{4+} ion, an entropy flux moves opposite to the electric current flow (hole); this phenomenon is referred to as spin entropy flow [89]. According to Eq. 11, the S_{Coeff} for $\text{Na}_{0.75}\text{CoO}_2$ (a common representative of the Na_xCoO_2 family with metallic conduction) is $249 \mu\text{V K}^{-1}$, which is quite comparable with the experimental measurements of $\sim 200 \mu\text{V K}^{-1}$ at 800 K [90].

Xiang et al. attempted to explain Na_xCoO_2 's high S_{Coeff} value using standard Boltzmann transport theory combined with spin-polarized DFT [92]. They found that S_{Coeff} was smaller when the system was set to be magnetically polarized, and interpreted the results as an alternative explanation for the suppression of S_{Coeff} in a magnetic field. According to their interpretation, the high S_{Coeff} and its suppression in high magnetic fields could be understood using the conventional transport theory applicable to other thermoelectric materials and that the unique thermoelectric properties of Na_xCoO_2 are due to its unusual band structure as manifested in the narrow manifold of t_{2g} bands in this system. However, the dependence of S_{Coeff} on Co's spin state (high spin vs. low spin) [93] still points to the spin entropy flow as the primary cause for high S_{Coeff} values.

What level of DFT?

Density functional theory (DFT) is one of the most common theoretical tools for probing strongly correlated TE materials such as Na_xCoO_2 . Within the DFT framework, the most basic approximation for the exchange–correlation functional, i.e., the local density approximation (LDA), in which the

exchange and correlation energy terms are fitted to those of a homogenous electron gas [94], fails to describe the electronic structures in highly correlated systems realistically [95]. The next most popular functional based on the general gradient approximation (GGA) [96], often, offers only a minor improvement [97]. The shortcoming stems from the fact the both LDA and GGA functionals tend to delocalize electrons over the lattice space. As such, each electron feels an average of the Coulombic potential. Consequently, for highly correlated materials, such as $\text{Na}_{0.75}\text{CoO}_2$, the significant Coulombic repulsion between localized electrons that results in charge disproportionation, are not correctly represented by LDA and GGA [83]. The thermoelectric effect, nonetheless, stems from charge disproportionation and needs an accurate theoretical description.

A standard solution for avoiding the delocalization problem of LDA and GGA functionals is to add an ad hoc Hubbard-like localized term to the LDA and GGA functionals. This approach is known as DFT + U (commonly referred to as LDA + U and GGA + U). Practically, in the DFT + U method [98, 99], one applies a Hubbard (U) and an exchange (J) terms to the localized d (or f) electrons. The delocalized electrons (s and p) are left unaltered as LDA and GGA correctly describe these delocalized electrons. To avoid the double-counting of the correlation part for localized electrons, another term—called the double-counting correction—is subtracted from the Hamiltonian. $U - J$, known as U_{eff} , determines the level of localization within the DFT + U implementation.

The U_{eff} value is not usually known a priori. Therefore, it is often chosen to replicate some experimental measurements [100]. For this reason, multiple values are usually reported in the literature for a given compound depending on the experimental values used as a benchmark, such as the band gap, formation enthalpy, or magnetic phase. In the case of Na_xCoO_2 , among the reported U and J values in the literature [101–103], all reproduce the charge disproportionation [104, 105] of the Co ions more or less accurately. That is to clearly distinguish Co^{2+} , Co^{3+} , and Co^{4+} from one another in terms of magnetization and partial density of states (PDOS). For instance, the more common value of $U_{\text{eff}} = 4 \text{ eV}$ is at a midpoint between the lower values of $\sim 3 \text{ eV}$ implemented Co^{3+} [106] and the higher values of $\sim 5 \text{ eV}$ implemented Co^{4+} [107–109].

The criticality of U_{eff}

As presented in the previous section, the exact choice of U_{eff} for Na_xCoO_2 remains somehow ambiguous. Here, we examine how the results of the DFT calculations with various U_{eff} value for $\text{Na}_{0.75}\text{CoO}_2$ (as a representative for the Na_xCoO_2 compound family) differ from one another. The problem to address is the arrangement of

Na ions (or equally Na vacancies) in the unit cell. Figure 6a shows the $\text{Na}_{0.75}\text{CoO}_2$ obtained with the LDA level of the theory [110]. In this structure, the unit cell contains a $\sqrt{3}a \times 4a \times 1c$ supercell in which the Na ions were arranged in rows of $3 \times \text{Na}_2$, progressively followed by a Na vacancy, a $3 \times \text{Na}_1$, and another Na vacancy. This structure has equal numbers of Na2 and Na1 ions ($\text{Na}_1/\text{Na}_2 = 1$). Figure 6(b) shows the Na arrangement obtained with $U_{\text{eff}} = 4$ eV (GGA + U formalism) [111]. Here, the irreducible unit cell has dimensions of $2\sqrt{3}a \times 2a \times 1c$ in which one-third of the Na ions occupied Na1 sites while two-third occupied Na2 sites ($\text{Na}_1/\text{Na}_2 = 0.5$) as the Na vacancies create a multi-vacancy cluster as marked by green enclosures. Moreover, Na ions at the Na2 sites were ever slightly off the oxygen axes conforming to the H1 structure [112]. Figure 6c shows the Na arrangement in $\text{Na}_{0.75}\text{CoO}_2$ calculated with $U_{\text{eff}} = 5$ eV (GGA + U formalism) [113]. Here, the ratio of Na_1/Na_2 is ~ 0.44 , where the Na ions in Na1 sites form ordered tri-Na1 droplets. The margin of the stability of the structure at Fig. 6c was, however, only ~ 2 meV lower than the competing structures which the authors had considered, implying that phase separation might occur at room temperature.

We can infer that the choice of U_{eff} is demonstrably critical in describing the arrangement of Na ions in $\text{Na}_{0.75}\text{CoO}_2$. Consequently, to validate the theoretical results, an accurate comparison with the experiment is required. This task is, however, easier said than done. Na is volatile, and its concentration in the sample may be smaller than the nominal value [114]. Furthermore, deciphering the real atomic environment at a given lattice point in Na_xCoO_2 experimentally, which is strongly dominated by the coordination environment, can be determined using the analysis of X-ray absorption near-edge spectra. However, such a measurement often is limited by the energy range of the instruments, rendering the interpretation of the results less than deterministic [115]. Obtaining a well-calibrated U_{eff} value for Na_xCoO_2 , therefore, remains a difficult task. Utilizing higher level theory such as Hartree–Fock/DFT hybrid functionals [116] or GW approximation [117] may offer more robust theoretical tools for probing Na_xCoO_2 and similar materials. Unfortunately, these methods are more computationally demanding than the standard or + U corrected DFT calculations.

Phonon calculations

As mentioned above, the efficiency of a TE generator depends on the ZT of the TE material, where κ can be further separated into lattice (κ_L) and electronic (κ_e) thermal conductivities. The latter is correlated with σ as shown by the Wiedemann–Franz law:

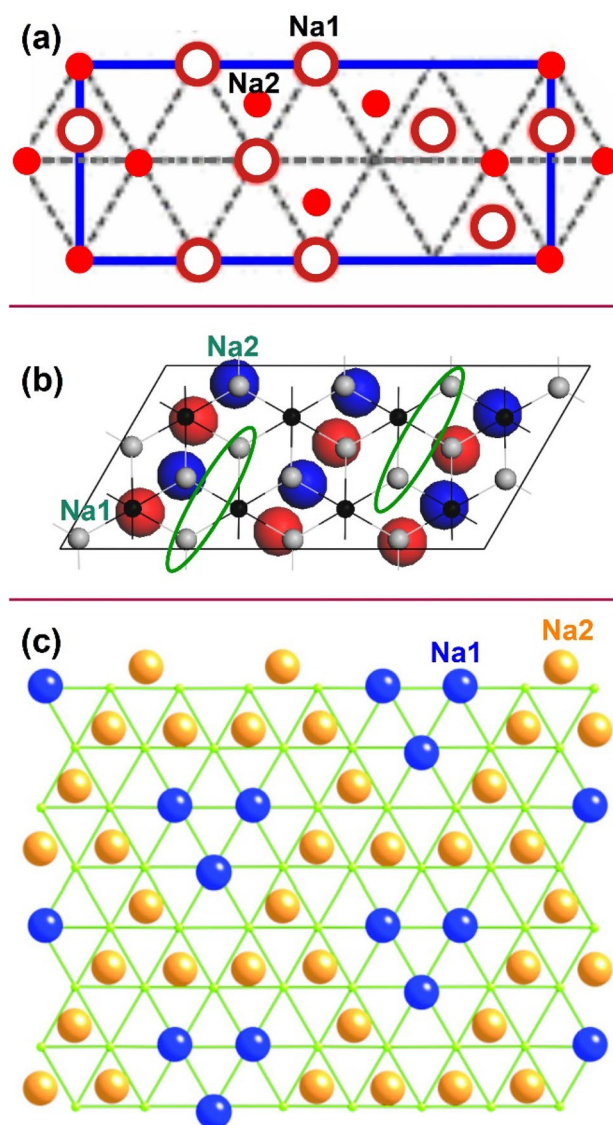


Fig. 6 The schematic presentation of Na ion arrangements in $\text{Na}_{0.75}\text{CoO}_2$ calculated with different U_{eff} values. **a** LDA calculations based on Zhang et al. [110]. The open circles denote those Na ions at $Z=0$, while solid circles denote those Na ions at $Z=0.5$ within the unit cell. **b** GGA + U ($U_{\text{eff}} = 4$ eV) calculations based on Assadi et al. [111]. Here, the color scheme is similar to that in Fig. 4. **c** GGA + U calculation based on Hinuma et al. [113] with $U_{\text{eff}} = 5$ eV. Here, the Na ions at $Z=0$ are at mirror locations of those at $Z=0.5$. The blue and gold spheres rather denote Na1 and Na2. Adapted after Refs. [110, 111, 113]. Copyrights 2005 American Physical Society, 2015 World Scientific, and 2008 American Institute of Physics

$$\kappa_e/\sigma = LT, \quad (12)$$

where L is the Lorenz number. Since κ_L is the only independent variable in ZT , lowering κ_L has been the most effective way to increase ZT in the past decades. An ideal TE material has the so-called “phonon-glass electron-crystal” (PGEC) property [118], with a high power factor

($PF = \sigma S_{\text{Coeff}}^2$) and a low κ_L . In this section, we will briefly summarize recent advances and challenges related to the ab initio description of κ_L .

Phonons and thermal conductivity

Debye first used quantized normal mode of the collective atomic vibrations to describe the specific heat of crystalline solids, giving birth to the concept of the phonon [119]. The phonon description of lattice vibrations has been spectacularly successful and has become a pillar of solid-state physics. In a harmonic oscillating lattice, phonons never interact, there is no lattice expansion, and κ_L approaches infinity. In a real lattice, the interatomic potential has anharmonic terms, which leads to interactions between phonon quasiparticles, thus resulting in a finite κ_L and lattice thermal expansion (some intriguing materials exhibit negative thermal expansion within a temperature range [120–123]). Peierls adapted the Boltzmann theory for the transport of gases to phonon “gas” to describe their population distributions driven out of equilibrium by a temperature gradient, formulating the Peierls–Boltzmann transport (PBTE) equation for determining phonon lifetimes and κ_L [124, 125]. The solution of the PBTE, a complex set of coupled integrodifferential equations, is a complicated task by itself. A variety of approximations have thus been introduced to develop an understanding of phonon driven thermal properties. For example, one can mention the Callaway and Klemens models of intrinsic phonon scattering and conductivity [126, 127]. Furthermore, Slack et al. developed a simple model for κ_L and a simple set of rules for its interpretation based on crystal complexity, average atomic mass, bonding strength, and anharmonicity [128, 129]. These are quantified in terms of a material’s Debye temperature and average Grüneisen parameter, which gives a measure of the speed of sound of the heat-carrying phonons and anharmonicity, respectively.

With the recent advances in theoretical and computational techniques and the exponentially increasing computational power, phonon band structure, group velocities, lifetimes, and thermal conductivity can be calculated from ab initio without ad hoc adjustable parameters. The solution of the PBTE has been achieved so substantially beyond the typical relaxation-time approximation, from variational methods [130] to self-consistent iterative procedures [131] and compressive sensing [132]. Moreover, realistic interatomic potentials for a variety of materials can be obtained from DFT [133]. The harmonic and anharmonic interatomic force constants (IFCs), as in Fig. 7 and Eq. 13, can be determined numerically either from DFT electronic-structure calculations based on supercell perturbations method [134] or from the linear response methods within density functional perturbation theory (DFPT) [135]. In the anharmonic case, as

shown in Fig. 7, the interatomic force is not proportional to the displacement, due to the third, fourth, and even higher order terms in the Taylor expansion of the potential energy V :

$$V = \sum_{ij,\alpha\beta} \frac{\partial^2 V}{\partial u_\alpha^i \partial u_\beta^j} \Delta u_\alpha^i \Delta u_\beta^j + \sum_{ijk,\alpha\beta\gamma} \frac{\partial^3 V}{\partial u_\alpha^i \partial u_\beta^j \partial u_\gamma^k} \Delta u_\alpha^i \Delta u_\beta^j \Delta u_\gamma^k + \sum_{ijkl,\alpha\beta\gamma\sigma} \frac{\partial^4 V}{\partial u_\alpha^i \partial u_\beta^j \partial u_\gamma^k \partial u_\sigma^l} \Delta u_\alpha^i \Delta u_\beta^j \Delta u_\gamma^k \Delta u_\sigma^l. \quad (13)$$

Nowadays, fully ab initio calculations of lattice thermal conductivity have become standard practice, owing to the availability of computational power and open-source code packages including but not limited to ShengBTE [136], Phono3py [137], PhonTS [131], and almaBTE [138]. However, these standard computations represent perfect and infinite single crystals. Real materials are finite and with imperfections, point defects like vacancies and interstitials, dislocations, and grain boundaries. In TE materials, defects are typically desired to tune the electronic band structure via doping and provide important scattering centers for phonons to lower κ_L . Defects add considerable complexity to the phonon calculations [139] and the prediction of κ_L in realistic materials. Ab initio calculations of phonon–phonon and phonon–defect interactions on the same footing are just becoming possible recently.

Realistic phonon calculations

A single site point defect changes the local structure and chemical bonding around it, providing a scattering center for phonons decreasing the thermal conductivity. This

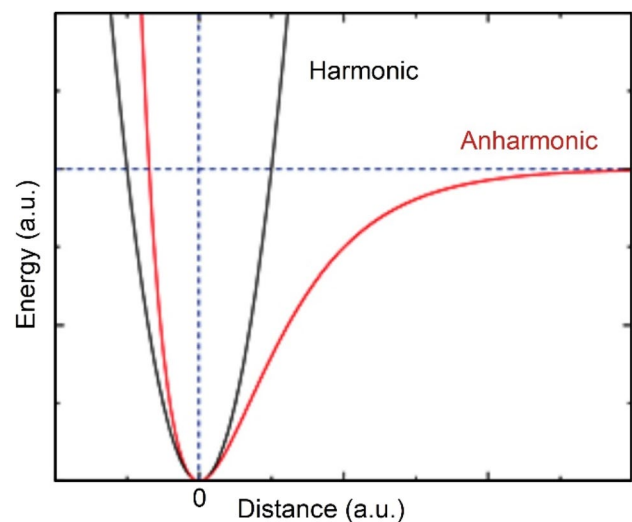


Fig. 7 Comparison of a harmonic and an anharmonic oscillator

thermal resistance mechanism can be accounted, to some extent, within the above-described software packages for calculating κ_L , often demonstrating excellent agreement with the measured data for high-quality crystals. However, the theory assumes that the point defects are randomly distributed in the lattice within the diluted limit, meaning that defects can scatter phonons without any correlation between them. As seen in Fig. 8, in the engineered materials with high point-defect concentration, this independent scattering model is questionable [140–142]. The inadequacy of this first-order perturbative description of point-defect scattering was shown in the recent work when comparing results from the first-order approximation with those of fully ab initio Green's function calculations of phonon scattering by vacancies and nitrogen substitution in diamond [141]. This work showed that including the variation of IFC induced by point defects and going beyond the first-order perturbations give much more reliable phonon-defect scattering prediction than the simple mass perturbation model.

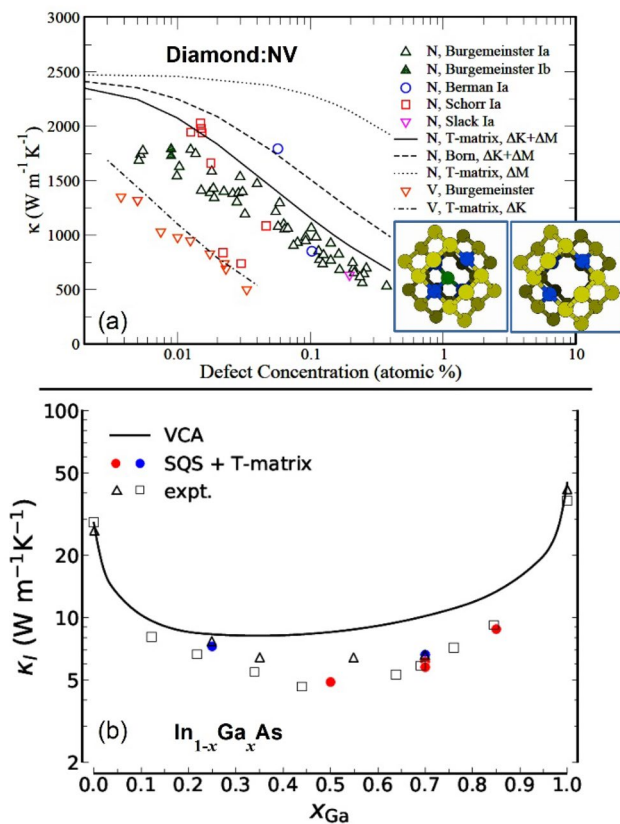


Fig. 8 **a** κ_L of diamond as a function of defect concentration. N and V stand for nitrogen and vacancy, respectively. The insets show the [100] projection view of the N impurity and vacancy defects after relaxation. Green: N atom. Blue: first coordination shell. Yellow: second and third coordination shells. **b** κ_L of $\text{In}_{1-x}\text{Ga}_x\text{As}$ calculated at 300 K with the VCA and with the special quasirandom structure approach. Adapted with permission from Refs. [141] and [142]. Copyrights 2014 and 2018 American Society of Physics

Further works have combined first-principles Green's function and PBTE methods to describe and predict κ_L in a variety of materials with different defect types (intrinsic vacancies and antisite, and substitutional dopants) [143, 144]. Among the intrinsic defects, vacancies are generally found to have the most potent effects on phonons scattering, due to the magnitude of the missing mass from vacancy centers and structural distortions. However, the “dilute limit” approximation is still assumed in most of the typical state-of-the-art phonon-defect calculations. Various methods have been employed for high concentrations of defects and coherent scattering mechanisms, such as the virtual crystal approximation (VCA) [145], supercell unfolding [142], and ab initio molecular dynamics (AIMD) simulations [146, 147].

One avenue in the search for low κ_L and high ZT is to examine very complex materials [148]; the ones that possess a variety of bonding patterns, rattling atoms in covalent cage structures, and many low-frequency optic phonon branches for the scattering of heat-carrying acoustic phonons. Computationally, such crystal complexity brings about significant challenges. In fact, ab initio PBTE methods have been recently used to explore complex unit cells of, for example, PbRb_4Br_6 or $\text{Cu}_{12}\text{Sb}_4\text{S}_{13}$ [132, 149]. The numerous vibrational degrees of freedom in the complex unit cells make the DFT calculations of the IFCs computationally tricky and increase the phase space for phonon–phonon interactions. These numerical bottlenecks would become less problematic as the computational power increases, offering a better understanding of the relevant physical mechanisms governing κ_L , and allowing better approximations to be made without much loss of precision in the near future.

A part of the state-of-the-art ab initio thermal transport methodologies is based on the phonon quasiparticle scattering picture within the quantum perturbation theory. Intrinsic phonon–phonon interactions are derived from the perturbations coming from higher order anharmonicity of the interatomic potential (derivatives of the interatomic potential with respect to each atomic displacement, see Eq. 13). For materials with extreme behaviors (such as strongly anharmonic) or in extreme conditions [like high T or pressure (P)], the ab initio methods derived from lowest order perturbation theory could show discrepancies between measured and calculated phonon transport properties. Materials that are about to or have undergone phase transition around or below the temperature of interest pose a crucial challenge as their lattice is highly anharmonic. Explicitly incorporating the thermal effects onto the anharmonic IFCs, beyond the quasiharmonic approximation, therefore, becomes necessary. Furthermore, including the fourth-order anharmonicity has been shown to be essential for κ_L in Si [150] at high temperature, and in PbTe, even at room temperature [151]. Molecular dynamics (MD) simulations of phonon transport

include all orders of the anharmonicity. MD, however, treats the atomic interactions classically; and AIMD remains prohibitively costly to tackle realistic system sizes.

Describing the lattice vibration and thermal transport at extreme T and P and near phase transitions driven by T or P will be the challenge for future *ab initio* phonon transport calculation and even to DFT in general. Phonons in materials near phase transitions can have localization as the mean-free path becomes comparable to their wavelength, constituting the Ioffe–Regel regime [152]. In this circumstance, a wave can no longer be readily defined. A localized vibrational state can become hybridized with propagating phonon states, resulting in resonant-like extended states with diffusive motion, not propagating, in nature. Perhaps, new quasiparticle picture like diffusons/locons [153, 154] in disordered materials will be needed to describe the lattice vibration phenomena in these extreme cases.

Recently, Hellman et al. have developed an accurate method, called the temperature-dependent effective potential (TDEP) technique, to determine the temperature-dependent anharmonic free energy, based on *ab initio* molecular dynamics followed by a mapping onto an effective model Hamiltonian describing the lattice dynamics. This method has been applied to various materials with dynamic instability, such as bcc Zr [155], and some strongly anharmonic materials, such as PbTe [156] and SnSe [157], which happen to be good thermoelectrics due to the very low thermal conductivity. Moreover, Zhou et al. calculated the electron–phonon interaction in the presence of soft-modes in SrTiO₃ perovskite from *ab initio* using (anharmonic) TDEP phonons [158]. The stochastic self-consistent harmonic approximation (SSCHA) is another novel development in the theoretical framework to study from *ab initio* the anharmonic properties of solids. SSCHA has been successfully applied to study the second-order structural phase transition and temperature-dependent anharmonic phonons primarily in various materials, such as the ferroelectric SnTe and GeTe [159], and the thermoelectric SnSe [159], as shown in Fig. 9.

For advanced TE materials, high-performance improvement needs to combine optimization of both the electronic and vibrational properties of the materials as these are tightly coupled. Thus, state-of-the-art numerical simulations of the TE materials need to incorporate electron–phonon interactions to improve our understanding of κ_L , S_{Coeff} , and σ as coupled properties. Numerical techniques have been built and developed recently for efficient calculation of electron–phonon interaction matrix elements from DFPT and quantum perturbation theory [160, 161]. These *ab initio* electron–phonon coupling has been examined and used to study transport phenomena in doped TE semiconductors [158, 162–165] and metals [166–168]. Rather than solving the transport equation for electron and the phonon separately, the solution of their coupled distribution equations would be the focus of future

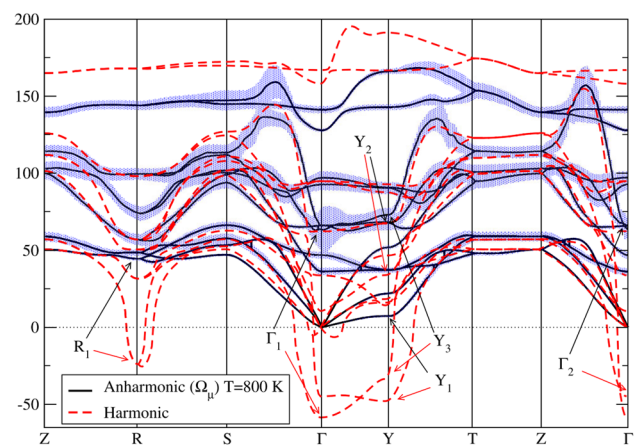


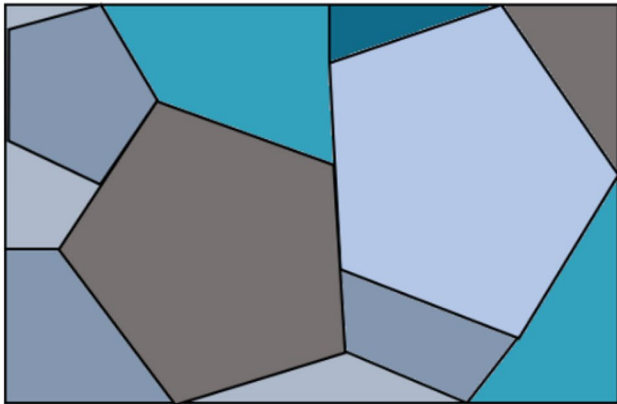
Fig. 9 Harmonic and anharmonic phonons in the Lorentzian approximation for SnSe. The length of the blue bars corresponds to the linewidth (full length of the line is the full width at half maximum). The calculations were performed with LDA on the experimental structure. Adapted with permission from Ref. [159]. Copyright 2019 American Society of Physics

calculations. These calculations shall be critically important in understanding the phonon-drag effects in TE materials, and the highly out-of-equilibrium electron and phonon dynamics in the ultrafast laser-based thermal spectroscopies.

Interfacial systems

Effective control of interfaces in thermoelectric materials is critical for improving their efficiency. In general, interfaces in thermoelectric devices are divided into two main types: (a) grain boundaries within single-phase materials and solid solutions; and (b) interfacial systems formed between different materials, e.g., superlattices or epitaxial layers. Figure 10 shows a schematic representation of grain boundaries in polycrystalline materials and multilayered heterostructures. Grain boundaries constitute the interfaces between grains in polycrystalline bulk materials. These grains may exhibit different atomic structures, crystal orientations, or different compositions. The role of grain boundaries is especially crucial in nanostructured materials, which are composed of small crystal grain sizes and exhibit a high density of grain boundaries. However, despite the numerous experimental observations of grain boundaries, their implications on transport properties are not entirely understood. Theoretical simulations are, therefore, a powerful tool to study the role of grain boundaries and interfacial systems in thermoelectric materials at the nano- and sub-nano-scale. Computer simulations can be used to discuss the stability of specific interfacial systems, in which vacancies or defects are commonly present (and serve as scattering centers, as explained in the previous section), the materials' behavior under mechanical

(a) Polycrystalline structure



(b) Multi-layered structure



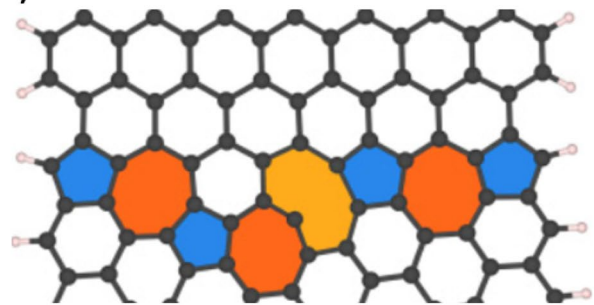
Fig. 10 Schematic representation of grain boundaries in **a** polycrystalline materials and **b** multilayered heterostructures. Variations in colors represent different crystallographic orientations in grains or different material compositions in solid solutions or heterostructures. Grain boundaries are denoted with black lines

strain or shear deformations, and their corresponding TE performance. Such theoretical investigations are, however, computationally expensive and have just recently become popular within the thermoelectric community. In this section, we will review some of the landmark studies in the field, focusing on the computational techniques employed.

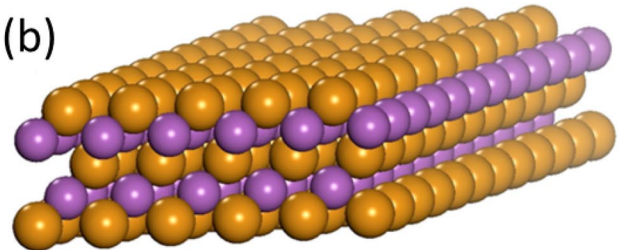
Nanostructuring and grain boundaries

From the theoretical perspective, electron and phonon transport in polycrystalline one-dimensional graphene nanoribbons and nanotubes was investigated by density functional tight-binding (DFTB) theory combined with non-equilibrium Green functions by Lehmann et al. [169]. The introduction of lattice imperfections such as dislocations was modeled by pentagons, heptagons, and octagons embedded within the hexagonal carbon nanostructures (Fig. 11a) which is suggested as an efficient method for enhancing the

(a)



(b)



(c)

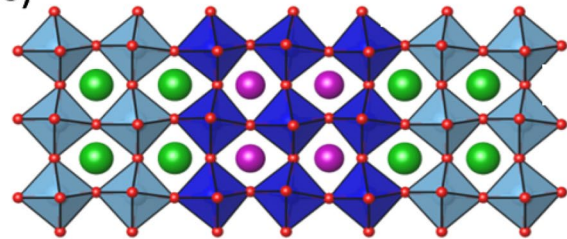


Fig. 11 Structures of **a** polycrystalline graphene nanoribbon with pentagon (blue shaded area), heptagon (orange), and octagon (yellow) defects obtained by joining two layers with an inclination angle of 24° [169], **b** Bi_2Te_3 one quintuple layer-thick slab (Te and Bi atoms are presented with orange and purple spheres, respectively) [173], and **c** p -type $\text{LaNiO}_3/\text{SrTiO}_3(001)$ superlattice with two p -type interfaces (La, Sr, and O atoms are purple, green, and red, respectively). Light and dark blue octahedra are centered around Ti and Ni ions, respectively) [180]. Adapted with permission from Refs. [169, 173, 180]. Copyrights 2015 and 2017 American Physical Society, and 2010 American Institute of Physics

TE effect. The computed S_{Coeff} exhibit values ~ -0.4 mV/K and ~ -0.6 mV/K in polycrystalline nanoribbons and nanotubes, respectively, in contrast to $S_{\text{Coeff}} > 0$ in the ideal graphene structures. Variations of the electronic and thermal properties in polycrystalline carbon-based systems give rise to an improved ZT by several orders of magnitude at room temperature.

Phosphorene (composed of a few-layer-thick black phosphorous) is another bidimensional material that exhibits highly anisotropic electrical and thermal conductances in single-crystal form. A combined DFT and self-energy correction (GW) study [170] demonstrated that the preferred directions for κ and σ in a phosphorene monolayer are orthogonal to one another. This results in an anisotropic ZT

that is large along the armchair direction, with ZT above 1 at 300 K and above 2 at 500 K, both for 60 ps relaxation time. However, in the experimentally processed material, the presence of defects may reduce the conductance and diminish the anisotropies.

In Si nanowires, simulations carried out by the ensemble Monte Carlo technique (EMC) [171] showed that the electrical conductivity decreases along with the cross section of the wire, while, on the other hand, S_{Coeff} increases as the wire cross section decreases. The calculated ZT in nanowires is 20–40 times more substantial compared to the bulk Si. The decrease in the κ_L due to strong phonon-boundary scattering can explain the remarkable enhancement in ZT . The above-described studies show that the formation of grain boundaries can be used to improve the thermoelectric efficiency by maximizing S_{Coeff} while decreasing the resistivity (ρ) and κ . On the other hand, grain boundaries can also affect the conductance negatively, reducing the anisotropy observed in single-crystalline counterparts.

Interfaces and heterostructures

Besides the recent progress in improving the performance of thermoelectric materials by modifying grain boundaries in nanostructured compounds, superlattices (formed by alternate stacking of two materials) have also shown potential to enhance the efficiency of TE energy conversion devices [172]. Ab initio DFT calculations showed that the slab formed by one atomic quintuple layer of Bi_2Te_3 (Fig. 11b) has the capacity to increase ZT to 7.15, which is ten times larger than for the bulk structure at room temperature [173]. The significant enhancement in ZT is caused by the changes in the valence band density from quantum confinement within the thin film.

Saha et al. studied HfN/ScN [174] and ZrN/ScN [175] metal/semiconductor superlattices constructed by stacking layers of both materials alternatively. The structure of these model interfaces and the computed electrostatic potentials as a function of the distance are depicted in Fig. 12. The p -type Schottky barrier height for the HfN/ScN of 0.77 eV is larger than the 0.34 eV in ZrN/ScN superlattices. The n -type barrier of the HfN/ScN superlattices is estimated to be 0.13 eV (versus 0.56 eV for ZrN/ScN), which suggests that these superlattice models are degenerate for electron transport along the cross plane. The lower barrier in HfN/ScN indicates the metallic conduction and lower S_{Coeff} compared to the ZrN counterpart. On the other hand, HfN/ScN superlattices present better κ_L than the ZrN-based models. These results point out the trade-off between S_{Coeff} and σ , suggesting that simultaneously increasing both parameters is still challenging in two-dimensional geometries.

Ab initio calculations have also been used to discuss the stability of solid-state TE with high cooling power density,

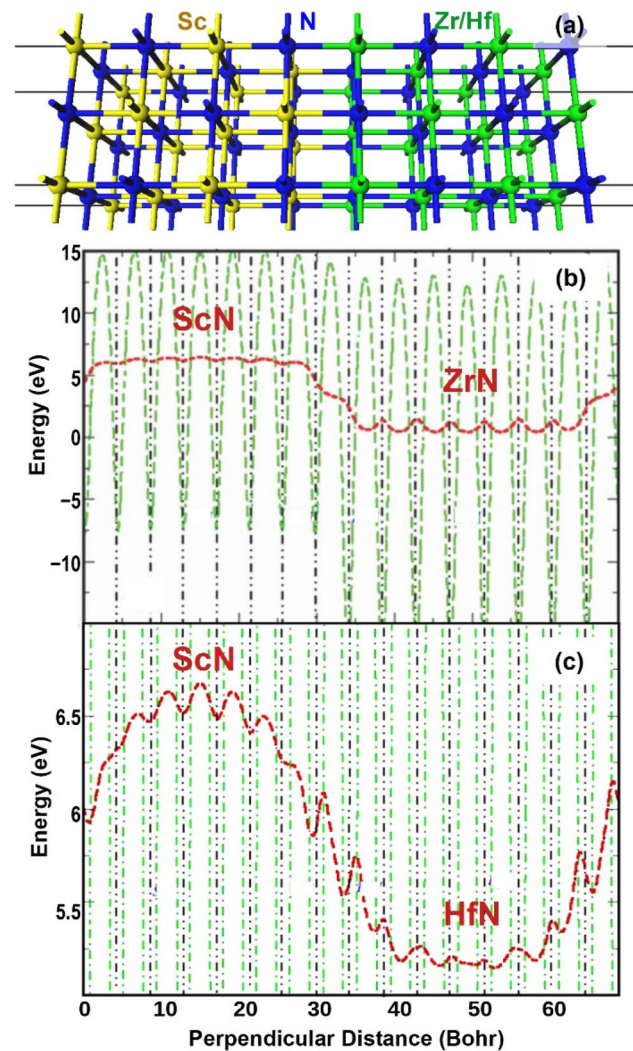


Fig. 12 a Metal–nitride interface structure formed between b ScN and ZrN [175] or c ScN and HfN [174]. b and c represent the planar average electrostatic potential (green dashed line) as a function of perpendicular distance from the ScN/ZrN and ScN/HfN interfaces, respectively. The red dashed line indicates the lattice-plane oscillations, which are filtered with the macroscopic averaging technique [182]. The vertical dashed black line represents the lattice planes. Adapted with permission from Refs.[174, 175]. Copyrights 2012 Institute of Physics and 2011 American Institute of Physics

such as epitaxial $\text{Ni}/\text{Bi}_2\text{Te}_3$, $\text{NiTe}/\text{Bi}_2\text{Te}_3$, $\text{Co}/\text{Bi}_2\text{Te}_3$, and $\text{CoTe}_2/\text{Bi}_2\text{Te}_3$ interfaces [176]. In these models, the metallic part is compressed/expanded by up to $\pm 10\%$ from its equilibrium structure to match the Bi_2Te_3 lattice parameters. All these interfaces were found to form stable Ohmic contacts. Other ab initio studies of epitaxial $\text{CoSb}_3/\text{TiCoSb}$ [177] and CoSb_3/Ti [178] interfaces discussed the stability, electronic structure, and mechanical properties of these model structures. These publications [177, 178] examined the atomic-level mechanical strain failure mechanisms in CoSb_3/Ti -based interfacial systems and found that the fracture takes

place in the CoSb_3 region, in line with experimental studies. The brittleness of the covalent Sb–Sb bond was compared with the more stable (ionic) Co–Sb bond in interfacial [177] and pure CoSb_3 models [179].

The study of epitaxial $\text{SrTiO}_3/\text{SrTi}_{1-x}\text{Nb}_x\text{O}_3$ ($0 \leq x \leq 0.5$) modeled by all-electron DFT showed that Nb doping induces metallicity into the originally insulating SrTiO_3 [181]. The Nb doping yields an increase in the carrier concentration while decreasing the thermoelectric response of the heterostructure. The exceptional agreement between the theory and experiment presented in this study demonstrates the high reliability of first-principles calculations for predicting S_{Coeff} within a wide-doping range. In SrTiO_3 interfaces forming epitaxial superlattices with LaNiO_3 (Fig. 11c), DFT + U calculations described how coupling interfaces of opposite polarity generate an electric field in the superlattice [180]. The analyses of the electronic transport and thermoelectric properties showed the anisotropic behavior of this interfacial model, which presents a large positive cross plane $S_{\text{Coeff}} \sim 135 \mu\text{V K}^{-1}$ and a ZT of 0.35 through the p -type superlattice at room temperature.

Understanding the atomic-level interfacial structure, mechanical stability, and electronic features are essential for the design of novel multi-layered materials with an enhanced thermoelectric ZT . These studies showed that the TE efficiency of superlattices could be largely improved compared to their bulk counterparts. The critical parameters for increasing the ZT in superlattices are optimizing the Schottky barrier for enhancing S_{Coeff} while retaining a high σ and reducing the cross plane κ at the interface. The mechanical properties are also an essential factor to consider for engineering applications, since the different thermal expansion coefficient at both sides of the interface may give rise to accumulated thermo-mechanical stresses that detrimentally form interfacial cracks.

Outlook

So far, we have discussed how Boltzmann transport equation, as implemented in BoltzTrap [24, 26] can offer solid predictions of the electronic transport properties of the thermoelectric materials. Furthermore, Peierls–Boltzmann transport (PBTE) equation, as implemented in ShengBTE code [136], can determine the phonon lifetimes and κ_L . These tools, coupled with the existing material structure databases, either based on computational [183–185] or experimental [186, 187] compilations, can automate the search for brand new thermoelectric materials through high-throughput calculations within a particular composition or structure space [188, 189]. Furthermore, interfaces based on the compounds in these databases can be automatically generated and screened using the MPIInterfaces tool [190]. The DFT and

transport calculations can be automated using Atomate software package [191] to run automatically, repair, and report the outcome. The outcome then can be searched for suitable intrinsic descriptors such as stability, band gap, flat-band feature, and S_{Coeff} to identify the most promising materials. Recently compounds such as $\text{Cu}_{12}\text{Sb}_4\text{S}_{13}$, $\text{Cu}_{26}\text{V}_2\text{Ge}_6\text{S}_{32}$ [192], ZnSnSb_2 , AgInS_2 , AgGaSe_2 , AgInSe_2 , and LiInTe_2 [193] have been predicted to be feasible thermoelectric materials via high-throughput calculations.

High-throughput calculations, although very powerful and predictive, come with some disadvantages. First, the uniformity of the computational settings among many chemical compositions under investigation may cause convergence issues in some compounds. Consequently, the generated data set may not be as accurate for all compounds or even miss some data points for which the DFT calculations catastrophically fail [194]. Moreover, regarding the transport properties, the assumption of a constant relaxation time across a set of compositions may not be realistic and thus is qualitative at best [195]. These problems restrict the capability of most high-throughput calculations in identifying the best thermoelectric materials. Consequently, the promising compounds discovered through such calculations should be further scrutinized with a higher level of theory. For instance, the use of the AMSET package [196] for the electronic transport calculations may remedy some of the shortcomings with the BoltzTrap method as it does not assume a constant relaxation time. AMSET, however, currently relies on a one-dimensional model of the averaged band structure, which limits its predictive power for materials with highly anisotropic band features.

An alternative to high-throughput calculations is to restrict the theoretical search to a handful number of compounds at each investigation—like the studies in Refs [36, 39] of Table 1, and Refs. [197, 198]—and fine-tune and customize the theoretical settings for the compounds under investigation. As one can see, the balance between the number of compounds investigated and the level of the accuracy is a trade-off to be determined by the constraints on the resources and the design of the search for new thermoelectric materials [199].

Conclusions

This review has highlighted the critical role that advanced computational techniques play in the understanding and design of thermoelectric materials. For instance, band structure calculations based on density functional theory with appropriate functional can aid in predicting the conventional thermoelectric materials operating based on a pudding-mold-shaped band near the Fermi level, such as CuAlO_2 , or strongly correlated thermoelectric materials that operate

based on Heikes formula for materials with mixed valency such as Na_xCoO_2 . Similarly, density functional theory can be employed to study the more complex interface effects at grain boundaries or heterostructures, for instance, in ScN/ZrN . Furthermore, the wavefunctions calculated by density functional theory can be used to predict the electronic transport (electrical conductivity, Seebeck coefficient, and electronic contribution to thermal conductivity) using Wannier Functions at minimum cost. Phonon dispersion calculations that can elucidate the lattice contribution to the thermal conductivity can be calculated with the Peierls–Boltzmann transport equation. As such, theoretical calculations can predict all properties affecting the thermoelectric performance of a given material or system. Consequently, the computational thermoelectric investigation can complement and assist in the analysis of experimental measurements; for instance, defect concentration, crystal structure, and grain boundary orientations. Moreover, such computational studies can explain the vital atomic-scale features and provide a fundamental understanding of the thermoelectric effect in novel materials for which detailed experimental characterization had not yet completed. Most importantly, such computational investigation can play a predictive role in the design of robust new thermoelectric materials.

Acknowledgements This work was supported by the Japanese Society for Promotion of Science. J.J.G.M. acknowledges financial support from the Postdoctoral Science Foundation of China under Grant no. 2018M643152. J.C. acknowledges the financial support from the Natural Science Foundation of Jiangsu Province under Grant number BK20180456.

Compliance with ethical standards

Conflict of interest The authors declare that we have no conflict of interest.

Open Access This article is licensed under a Creative Commons Attribution 4.0 International License, which permits use, sharing, adaptation, distribution and reproduction in any medium or format, as long as you give appropriate credit to the original author(s) and the source, provide a link to the Creative Commons licence, and indicate if changes were made. The images or other third party material in this article are included in the article's Creative Commons licence, unless indicated otherwise in a credit line to the material. If material is not included in the article's Creative Commons licence and your intended use is not permitted by statutory regulation or exceeds the permitted use, you will need to obtain permission directly from the copyright holder. To view a copy of this licence, visit <http://creativecommons.org/licenses/by/4.0/>.

References

1. Forman, C., Muritala, I.K., Pardemann, R., Meyer, B.: Estimating the global waste heat potential. *Renew. Sust. Energy Rev.* **57**, 1568–1579 (2016)

2. Seebeck, T.J.: Ueber die magnetische Polarisation der Metalle und Erze durch Temperatur-Differenz. *Ann. Phys.* **82**(2), 133–160 (1826)
3. Mele, P., Kamei, H., Yasumune, H., Matsumoto, K., Miyazaki, K.: Development of thermoelectric module based on dense $\text{Ca}_3\text{Co}_2\text{O}_9$ and $\text{Zn}_{0.98}\text{Al}_{0.02}\text{O}$ legs. *Met. Mater. Int.* **20**(2), 389–397 (2014)
4. Saini, S., Mele, P., Miyazaki, K., Tiwari, A.: On-chip thermoelectric module comprised of oxide thin film legs. *Energy Convers. Manag.* **114**, 251–257 (2016)
5. Stevens, R.J., Weinstein, S.J., Koppula, K.S.: Theoretical limits of thermoelectric power generation from exhaust gases. *Appl. Energy* **133**, 80–88 (2014)
6. Twaha, S., Zhu, J., Yan, Y., Li, B.: A comprehensive review of thermoelectric technology: materials, applications, modelling and performance improvement. *Renew. Sust. Energy. Rev.* **65**, 698–726 (2016)
7. Li, Q., Shirazi, A., Zheng, C., Rosengarten, G., Scott, J.A., Taylor, R.A.: Energy concentration limits in solar thermal heating applications. *Energy* **96**, 253–267 (2016)
8. Chen, G., Dresselhaus, M.S., Dresselhaus, G., Fleurial, J.P., Caillat, T.: Recent developments in thermoelectric materials. *Int. Mater. Rev.* **48**(1), 45–66 (2003)
9. Minnich, A.J., Dresselhaus, M.S., Ren, Z.F., Chen, G.: Bulk nanostructured thermoelectric materials: current research and future prospects. *Energy Environ. Sci.* **2**(5), 466–479 (2009)
10. Lu, W., Xiao, R., Yang, J., Li, H., Zhang, W.: Data mining-aided materials discovery and optimization. *J. Materiomics* **3**(3), 191–201 (2017)
11. Hao, S., Draid, V.P., Kanatzidis, M.G., Wolverton, C.: Computational strategies for design and discovery of nanostructured thermoelectrics. *Npj Comput. Mater.* **5**(1), 58 (2019)
12. Shi, Y., Wang, Y., Mei, D., Feng, B., Chen, Z.: Design and fabrication of wearable thermoelectric generator device for heat harvesting. *IEEE Robot. Autom. Lett.* **3**(1), 373–378 (2018)
13. Tritt, T.M., Subramanian, M.A.: Thermoelectric materials, phenomena, and applications: a bird's eye view. *MRS Bull.* **31**(3), 188–194 (2006)
14. Stratton, R.: Diffusion of hot and cold electrons in semiconductor barriers. *Phys. Rev.* **126**(6), 2002 (1962)
15. Assadi, M.H.N., Mele, P., Fronzi, M.: Suppression of magnetism and Seebeck effect in $\text{Na}_{0.875}\text{CoO}_2$ induced by SbCo dopants. *Mater. Renew. Sustain. Energy* **9**(1), 5 (2020)
16. Jonson, M., Mahan, G.D.: Mott's formula for the thermopower and the Wiedemann-Franz law. *Phys. Rev. B* **21**(10), 4223–4229 (1980)
17. Movshovich, R., Jaime, M., Thompson, J.D., Petrovic, C., Fisk, Z., Pagliuso, P.G., Sarrao, J.L.: Unconventional Superconductivity in CeIrIn_5 and CeCoIn_5 : specific heat and thermal conductivity studies. *Phys. Rev. Lett.* **86**(22), 5152–5155 (2001)
18. Gelbstein, Y.: $\text{Pb}_{1-x}\text{Sn}_x\text{Te}$ alloys: application considerations. *J. Electron. Mater.* **40**(5), 533–536 (2011)
19. Saleh, S.: Enhancement of the power factor of $\text{Pb}_{1-x}\text{Sn}_x\text{Te}$ ($0.00 \geq x \geq 0.08$) alloys. *Philos. Mag.* **94**(28), 3183–3194 (2014)
20. Bhandari, C., Rowe, D.: High-temperature thermal transport in heavily doped small-grain-size lead telluride. *Appl. Phys. A* **37**(3), 175–178 (1985)
21. Zebarjadi, M., Esfarjani, K., Dresselhaus, M., Ren, Z., Chen, G.: Perspectives on thermoelectrics: from fundamentals to device applications. *Energy Environ. Sci.* **5**(1), 5147–5162 (2012)
22. Cutler, M., Mott, N.F.: Observation of Anderson localization in an electron gas. *Phys. Rev.* **181**(3), 1336–1340 (1969)

23. Scheidemantel, T.J., Ambrosch-Draxl, C., Thonhauser, T., Bading, J.V., Sofo, J.O.: Transport coefficients from first-principles calculations. *Phys. Rev. B* **68**(12), 125210 (2003)
24. Madsen, G.K., Singh, D.J.: BoltzTraP. A code for calculating band-structure dependent quantities. *Comput. Phys. Commun.* **175**(1), 67–71 (2006)
25. Landauer, R.: Electrical transport in open and closed systems. *Z. Phys.* **68**(2–3), 217–228 (1987)
26. Madsen, G.K.H., Carrete, J., Verstraete, M.J.: BoltzTraP2, a program for interpolating band structures and calculating semi-classical transport coefficients. *Comput. Phys. Commun.* **231**, 140–145 (2018)
27. Bulusu, A., Walker, D.: Review of electronic transport models for thermoelectric materials. *Superlattices Microstruct.* **44**(1), 1–36 (2008)
28. Woods, L.: Limitations of Boltzmann’s kinetic equation. *Proc. R. Soc. Ser. A* **464**(2095), 1923–1940 (2008)
29. Chen, L.-Y., Su, Z.-B.: Quantum Boltzmann equation and Kubo formula for electronic transport in solids. *Phys. Rev. B* **40**(13), 9309–9311 (1989)
30. Thouless, D.: Relation between the Kubo-Greenwood formula and the Boltzmann equation for electrical conductivity. *Philos. Mag.* **32**(4), 877–879 (1975)
31. Olvera, A., Shi, G., Djieutedjeu, H., Page, A., Uher, C., Kioupakakis, E., Poudeu, P.F.: $\text{Pb}_7\text{Bi}_4\text{Se}_{13}$: a lillianite homologue with promising thermoelectric properties. *Inorg. Chem.* **54**(3), 746–755 (2014)
32. Lee, S.-C.: Robust mechanical stability, electronic structure, magnetism and thermoelectric properties of CoFeMnSb quaternary Heusler alloy: a first principle study. *J. Alloy. Compd.* **742**, 903–909 (2018)
33. Khan, W., Hussain, S., Minar, J., Azam, S.: Electronic and thermoelectric properties of ternary chalcogenide semiconductors: first principles study. *J. Electron. Mater.* **47**(2), 1131–1139 (2018)
34. Joshi, H., Rai, D., Verma, K., Bhamu, K., Thapa, R.: Thermoelectric properties of tetragonal half-Heusler compounds, TiXSb ($X = \text{Ge}, \text{Si}$): a probe from Density Functional Theory (DFT). *J. Alloy. Compd.* **726**, 1155–1160 (2017)
35. Ramay, S.M., Hassan, M., Mahmood, Q., Mahmood, A.: The study of electronic, magnetic, magneto-optical and thermoelectric properties of XC_2O_4 ($X = \text{Zn}, \text{Cd}$) through modified Becke and Johnson potential scheme (mBJ). *Curr. Appl. Phys.* **17**(8), 1038–1045 (2017)
36. Mahmood, Q., Hassan, M., Ahmad, S.H.A., Bhamu, K.C., Mahmood, A., Ramay, S.M.: Study of electronic, magnetic and thermoelectric properties of AV_2O_4 ($A = \text{Zn}, \text{Cd}, \text{Hg}$) by using DFT approach. *J. Phys. Chem. Solids* **128**, 283–290 (2019)
37. Dar, S.A., Srivastava, V., Sakalle, U.K.: Structural, elastic, mechanical, electronic, magnetic, thermoelectric and thermodynamic investigation of half metallic double perovskite oxide $\text{Sr}_2\text{MnTaO}_6$. *J. Mag. Mater.* **484**, 298–306 (2019)
38. Noor, N.A., Mahmood, Q., Rashid, M., Ul Haq, B., Laref, A., Ahmad, S.A.: Ab-initio study of thermodynamic stability, thermoelectric and optical properties of perovskites ATiO_3 ($A = \text{Pb}, \text{Sn}$). *J. Solid State Chem.* **263**, 115–122 (2018)
39. Noor, N., Saddique, M.B., Haq, B.U., Laref, A., Rashid, M.: Investigations of half-metallic ferromagnetism and thermoelectric properties of cubic XCrO_3 ($X = \text{Ca}, \text{Sr}, \text{Ba}$) compounds via first-principles approaches. *Phys. Lett. A* **382**(42–43), 3095–3102 (2018)
40. Adewale, A.A., Chik, A., Zaki, R.M., Pa, F.C., Yeoh, C.K., Jamil, N.H.: Enhancement of thermoelectric figure of merit of $\text{SrTi}_{0.92}\text{R}_{0.08}\text{O}_3$ ($R = \text{Ta}, \text{Ho}$). *AIP Conf. Proc.* **2030**(1), 020196 (2018)
41. Singh, S., Kumar, D., Pandey, S.K.: Experimental and theoretical investigations of thermoelectric properties of $\text{La}_{0.82}\text{Ba}_{0.18}\text{CoO}_3$ compound in high temperature region. *Phys. Lett. A* **381**(36), 3101–3106 (2017)
42. Marzari, N., Vanderbilt, D.: Maximally localized generalized Wannier functions for composite energy bands. *Phys. Rev. B* **56**(20), 12847–12865 (1997)
43. Calzolari, A., Marzari, N., Souza, I., Nardelli, M.B.: Ab initio transport properties of nanostructures from maximally localized Wannier functions. *Phys. Rev. B* **69**(3), 035108 (2004)
44. Pizzi, G., Volja, D., Kozinsky, B., Fornari, M., Marzari, N.: BoltzWann: a code for the evaluation of thermoelectric and electronic transport properties with a maximally-localized Wannier functions basis. *Comput. Phys. Commun.* **185**(1), 422–429 (2014)
45. Kaliaperumal, S., Balan, P., Ramaswamy, M.: Electronic and thermoelectric properties of SrTiO_3 . *Current Smart Mater.* **2**(1), 73–79 (2017)
46. Mori, K., Sakakibara, H., Usui, H., Kuroki, K.: Ideal band shape in the potential thermoelectric material CuAlO_2 : comparison to Na_xCoO_2 . *Phys. Rev. B* **88**(7), 075141 (2013)
47. Kopnin, N., Heikkilä, T., Volovik, G.: High-temperature surface superconductivity in topological flat-band systems. *Phys. Rev. B* **83**(22), 220503 (2011)
48. Shaginyan, V., Khodel, V.: Superfluidity in system with fermion condensate. *JETP Lett.* **51**(9), 553–555 (1990)
49. Volovik, G.: A new class of normal Fermi liquids. *JETP Lett.* **53**(4), 222–225 (1991)
50. Shaginyan, V., Amusia, M.Y., Msezane, A., Popov, K.: Scaling behavior of heavy fermion metals. *Phys. Rep.* **492**(2–3), 31–109 (2010)
51. Gulácsi, Z., Kampf, A., Vollhardt, D.: Route to ferromagnetism in organic polymers. *Phys. Rev. Lett.* **105**(26), 266403 (2010)
52. Dóra, B., Kailasvuori, J., Moessner, R.: Lattice generalization of the Dirac equation to general spin and the role of the flat band. *Phys. Rev. B* **84**(19), 195422 (2011)
53. Ishii, H., Nakayama, T.: Quantum electron transport in finite-size flat-band Kagome Lattice systems. *AIP Conf. Proc.* **772**(1), 1285–1286 (2005)
54. Isaacs, E.B., Wolverson, C.: Remarkable thermoelectric performance in BaPdS_2 via pudding-mold band structure, band convergence, and ultralow lattice thermal conductivity. *Phys. Rev. Mater.* **3**(1), 015403 (2019)
55. Kuroki, K., Arita, R.: “Pudding Mold” band drives large thermopower in Na_xCoO_2 . *J. Phys. Soc. Jpn.* **76**(8), 083707 (2007)
56. Koumoto, K., Mori, T.: *Thermoelectric Nanomaterials: Materials Design and Applications*. Springer, New York (2013)
57. Ohkubo, I., Mori, T.: Two-dimensional layered complex nitrides as a new class of thermoelectric materials. *Chem. Mater.* **26**(8), 2532–2536 (2014)
58. Ohkubo, I., Mori, T.: Origin of projected excellent thermoelectric transport properties in d^0 -electron AMN_2 ($A = \text{Sr}$ or Ba ; $M = \text{Ti}, \text{Zr}, \text{Hf}$) layered complex metal nitrides. *Eur. J. Inorg. Chem.* **2015**(22), 3715–3722 (2015)
59. Ohkubo, I., Mori, T.: Three-dimensionality of electronic structures and thermoelectric transport in SrZrN_2 and SrHfN_2 layered complex metal nitrides. *Inorg. Chem.* **53**(17), 8979–8984 (2014)
60. Ohkubo, I., Mori, T.: Anisotropic anomalies of thermoelectric transport properties and electronic structures in layered complex nitrides AMN_2 ($A = \text{Na}, \text{Cu}$; $M = \text{Ta}, \text{Nb}$). *Chem. Mater.* **27**(21), 7265–7275 (2015)
61. Nakamura, Y., Uchida, S.: Anisotropic transport properties of single-crystal $\text{La}_{2-x}\text{Sr}_x\text{CuO}_4$: evidence for the dimensional crossover. *Phys. Rev. B* **47**(13), 8369–8372 (1993)

62. Maeno, Y., Hashimoto, H., Yoshida, K., Nishizaki, S., Fujita, T., Bednorz, J., Lichtenberg, F.: Superconductivity in a layered perovskite without copper. *Nature* **372**(6506), 532–534 (1994)
63. Sugiura, K., Ohta, H., Nakagawa, S.-I., Huang, R., Ikuhara, Y., Nomura, K., Hosono, H., Koumoto, K.: Anisotropic carrier transport properties in layered cobaltate epitaxial films grown by reactive solid-phase epitaxy. *Appl. Phys. Lett.* **94**(15), 152105 (2009)
64. Assadi, M.H.N., Shigeta, Y.: The effect of octahedral distortions on the electronic properties and magnetic interactions in O3 NaTMO₂ compounds (TM = Ti–Ni & Zr–Pd). *RSC Adv.* **8**(25), 13842–13849 (2018)
65. Ohkubo, I., Mori, T.: Anisotropic thermoelectric properties in layered complex nitrides with α -NaFeO₂-type structure. *APL Mater.* **4**(10), 104808 (2016)
66. Tang, G.D., Xu, X.N., Tang, C.P., Wang, Z.H., He, Y., Qiu, L., Lv, L.Y., Xing, L., Du, Y.W.: The spin-entropy enhancement induced by Ce doping in Ca₃Co₄O_{9+ δ} . *EPL* **91**(1), 17002 (2010)
67. Pourret, A., Malone, L., Antunes, A.B., Yadav, C., Paulose, P., Fauqué, B., Behnia, K.: Strong correlation and low carrier density in Fe_{1+y}Te_{0.6}Se_{0.4} as seen from its thermoelectric response. *Phys. Rev. B* **83**(2), 020504 (2011)
68. Terasaki, I., Sasago, Y., Uchinokura, K.: Large thermoelectric power in NaCo₂O₄ single crystals. *Phys. Rev. B* **56**(20), R12685–R12687 (1997)
69. Terasaki, I., Tsukada, I., Iguchi, Y.: Impurity-induced transition and impurity-enhanced thermopower in the thermoelectric oxide NaCo_{2-x}Cu_xO₄. *Phys. Rev. B* **65**(19), 195106 (2002)
70. Foo, M.L., Wang, Y., Watauchi, S., Zandbergen, H., He, T., Cava, R., Ong, N.: Charge ordering, commensurability, and metallicity in the phase diagram of the layered Na_xCoO₂. *Phys. Rev. Lett.* **92**(24), 247001 (2004)
71. Haerter, J.O., Peterson, M.R., Shastry, B.S.: Strong correlations produce the Curie-Weiss phase of Na_xCoO₂. *Phys. Rev. Lett.* **97**(22), 226402 (2006)
72. Wang, Y., Rogado, N.S., Cava, R., Ong, N.: Spin entropy as the likely source of enhanced thermopower in Na_xCo₂O₄. *Nature* **423**(6938), 425–428 (2003)
73. Takeuchi, T., Matoba, M., Aharen, T., Itoh, M.: Magnetic anomalies in Na_xCoO₂ (x = 0.75). *Phys. B* **312**, 719–720 (2002)
74. Yoshizumi, D., Muraoka, Y., Okamoto, Y., Kiuchi, Y., Yamaura, J.-I., Mochizuki, M., Ogata, M., Hiroi, Z.: Precise control of band filling in Na_xCoO₂. *J. Phys. Soc. Jpn.* **76**(6), 063705–063705 (2007)
75. Fergus, J.W.: Oxide materials for high temperature thermoelectric energy conversion. *J. Eur. Ceram. Soc.* **32**(3), 525–540 (2012)
76. Weller, M., Sacchetti, A., Ott, H., Mattenberger, K., Batlogg, B.: Melting of the Na layers in solid Na_{0.8}CoO₂. *Phys. Rev. Lett.* **102**(5), 056401 (2009)
77. Nagira, T., Ito, M., Katsuyama, S., Majima, K., Nagai, H.: Thermoelectric properties of (Na_{1-y}M_y)_xCo₂O₄ (M = K, Sr, Y, Nd, Sm and Yb; y=0.01 similar to 0.35). *J. Alloy. Compd.* **348**(1–2), 263–269 (2003)
78. Ozgur, U., Gu, X., Chevtchenko, S., Spradlin, J., Cho, S.J., Morkoc, H., Pollak, F.H., Everitt, H.O., Nemeth, B., Nause, J.E.: Thermal conductivity of bulk ZnO after different thermal treatments. *J. Electron. Mater.* **35**(4), 550–555 (2006)
79. Kawata, T., Iguchi, Y., Itoh, T., Takahata, K., Terasaki, I.: Na-site substitution effects on the thermoelectric properties of NaCo₂O₄. *Phys. Rev. B* **60**(15), 10584–10587 (1999)
80. Motohashi, T., Naujalis, E., Ueda, R., Isawa, K., Karppinen, M., Yamauchi, H.: Simultaneously enhanced thermoelectric power and reduced resistivity of Na_xCo₂O₄ by controlling Na nonstoichiometry. *Appl. Phys. Lett.* **79**(10), 1480–1482 (2001)
81. Cui, L., Zhao, Y.G., Zhang, G.M., Zhang, W.Y., Guo, Z.P., Ren, W., Zhang, X.P., Zhu, M.H.: Structural and electronic transport properties of Na_xCoO₂. *J. Alloy. Compd.* **426**(1), 72–75 (2006)
82. Goodenough, J.B.: Metallic oxides. *Prog. Solid State Chem.* **5**, 145–399 (1971)
83. Assadi, M.H.N., Li, S., Yu, A.B.: Selecting the suitable dopants: electronic structures of transition metal and rare earth doped thermoelectric sodium cobaltate. *RSC Adv.* **3**(5), 1442–1449 (2013)
84. Assadi, M.H.N., Li, S., Zheng, R.K., Ringer, S.P., Yu, A.B.: Magnetic, electrochemical and thermoelectric properties of P2-Na_x(Co_{7/8}Sb_{1/8})O₂. *Chem. Phys. Lett.* **687**, 233–237 (2017)
85. Terasaki, I.: High-temperature oxide thermoelectrics. *J. Appl. Phys.* **110**(5), 053705 (2011)
86. Koshibae, W., Tsutsui, K., Maekawa, S.: Thermopower in cobalt oxides. *Phys. Rev. B* **62**(11), 6869–6872 (2000)
87. Heikes, R.R., Ure, R.W.: *Thermoelectricity: Science and Engineering*. Interscience Publishers, New York (1961)
88. Chaikin, P.M., Beni, G.: Thermopower in the correlated hopping regime. *Phys. Rev. B* **13**(2), 647–651 (1976)
89. Terasaki, I., Shibusaki, S., Yoshida, S., Kobayashi, W.: Spin state control of the perovskite Rh/Co oxides. *Materials* **3**(2), 786–799 (2010)
90. Fujita, K., Mochida, T., Nakamura, K.: High-temperature thermoelectric properties of Na_xCoO_{2- δ} single crystals. *Jpn. J. Appl. Phys.* **40**(Part 1, No. 7), 4644–4647 (2001)
91. Assadi, M.H.N.: Na site doping a pathway for enhanced thermoelectric performance in Na_{1-x}CoO₂; the case of Gd and Yb dopants. *J. Phys. Condens. Matter* **32**(12), 125502 (2019)
92. Xiang, H., Singh, D.: Suppression of thermopower of Na_xCoO₂ by an external magnetic field: Boltzmann transport combined with spin-polarized density functional theory. *Phys. Rev. B* **76**(19), 195111 (2007)
93. Shu, G., Chou, F.: Ferrimagnetic ordering and spin entropy of field-dependent intermediate spins in Na_{0.82}CoO₂. *Phys. Rev. B* **93**(14), 140402 (2016)
94. Parr, R.G., Yang, W.: *Density-functional theory of the electronic structure of molecules*. *Annu. Rev. Phys. Chem.* **46**(1), 701–728 (1995)
95. Muscat, J., Wander, A., Harrison, N.: On the prediction of band gaps from hybrid functional theory. *Chem. Phys. Lett.* **342**(3–4), 397–401 (2001)
96. Perdew, J.P., Chevary, J.A., Vosko, S.H., Jackson, K.A., Pederson, M.R., Singh, D.J., Fiolhais, C.: Atoms, molecules, solids, and surfaces: applications of the generalized gradient approximation for exchange and correlation. *Phys. Rev. B* **46**(11), 6671 (1992)
97. Haas, P., Tran, F., Blaha, P., Schwarz, K., Laskowski, R.: Insight into the performance of GGA functionals for solid-state calculations. *Phys. Rev. B* **80**(19), 195109 (2009)
98. Liechtenstein, A.I., Anisimov, V.I., Zaanen, J.: Density-functional theory and strong interactions: orbital ordering in Mott-Hubbard insulators. *Phys. Rev. B* **52**(8), R5467–R5470 (1995)
99. Dudarev, S., Botton, G., Savrasov, S., Humphreys, C., Sutton, A.: Electron-energy-loss spectra and the structural stability of nickel oxide: An LSDA+U study. *Phys. Rev. B* **57**(3), 1505–1509 (1998)
100. Petukhov, A.G., Mazin, I.I., Chioncel, L., Liechtenstein, A.I.: Correlated metals and the LDA+U method. *Phys. Rev. B* **67**(15), 153106 (2003)
101. Lee, K.-W., Pickett, W.: Charge and spin ordering in insulating NaOCoO₂: effects of correlation and symmetry. *Phys. Rev. Lett.* **96**(9), 096403 (2006)
102. Hinuma, Y., Meng, Y.S., Ceder, G.: Temperature-concentration phase diagram of P2-Na_xCoO₂ from first-principles calculations. *Phys. Rev. B* **77**(22), 224111 (2008)

103. Molenda, J., Baster, D., Molenda, M., Świerczek, K., Tobola, J.: Anomaly in the electronic structure of the $\text{Na}_x\text{CoO}_{2-y}$ cathode as a source of its step-like discharge curve. *Phys. Chem. Chem. Phys.* **16**(28), 14845–14857 (2014)
104. Mukhamedshin, I., Alloul, H.: Na order and Co charge disproportionation in Na_xCoO_2 . *Phys. B* **460**, 58–63 (2015)
105. Mukhamedshin, I., Dooglav, A., Krivenko, S., Alloul, H.: Evolution of Co charge disproportionation with Na order in Na_xCoO_2 . *Phys. Rev. B* **90**(11), 115151 (2014)
106. Jain, A., Hautier, G., Ong, S.P., Moore, C.J., Fischer, C.C., Persson, K.A., Ceder, G.: Formation enthalpies by mixing GGA and GGA+U calculations. *Phys. Rev. B* **84**(4), 045115 (2011)
107. Aykol, M., Wolverton, C.: Local environment dependent GGA+U method for accurate thermochemistry of transition metal compounds. *Phys. Rev. B* **90**(11), 115105 (2014)
108. Aykol, M., Kim, S., Wolverton, C.: van der Waals interactions in layered lithium cobalt oxides. *J. Phys. Chem. C* **119**(33), 19053–19058 (2015)
109. Zhao, Z., Yao, J., Sun, B., Zhong, S., Lei, X., Xu, B., Ouyang, C.: First-principles identification of spinel CaCo_2O_4 as a promising cathode material for Ca-ion batteries. *Solid State Ion.* **326**, 145–149 (2018)
110. Zhang, P., Capaz, R.B., Cohen, M.L., Louie, S.G.: Theory of sodium ordering in Na_xCoO_2 . *Phys. Rev. B* **71**(15), 153102 (2005)
111. Assadi, M., Katayama-Yoshida, H.: Interplay between magnetism and Na concentration in Na_xCoO_2 . *Funct. Mater. Lett.* **8**(03), 1540016 (2015)
112. Huang, Q., Lynn, J.W., Toby, B.H., Foo, M.L., Cava, R.J.: Characterization of the structural transition in $\text{Na}_{0.75}\text{CoO}_2$. *J. Phys. Condens. Matter* **17**(12), 1831–1840 (2005)
113. Meng, Y.S., Hinuma, Y., Ceder, G.: An investigation of the sodium patterning in Na_xCoO_2 ($0.5 \leq x \leq 1$) by density functional theory methods. *J. Chem. Phys.* **128**(10), 104708 (2008)
114. Cushing, B.L., Wiley, J.B.: Improved synthetic routes to layered Na_xCoO_2 Oxides. *Synth. React. Inorg. M.* **29**(7), 1199–1207 (1999)
115. Penner-Hahn, J.E.: X-ray absorption spectroscopy. In: McCleverty, J.A., Meyer, T.J. (eds.) *Comprehensive Coordination Chemistry II*, pp. 159–186. Pergamon, Oxford (2003)
116. Assadi, M., Li, S., Zheng, R., Ringer, S., Yu, A.: In-plane antiferromagnetism in $\text{Na}_{0.5}\text{CoO}_2$ induced by Sb_{Co} dopants. *arXiv Preprint*, arXiv:1211.6167 (2012)
117. Seo, D.-H., Urban, A., Ceder, G.: Calibrating transition-metal energy levels and oxygen bands in first-principles calculations: accurate prediction of redox potentials and charge transfer in lithium transition-metal oxides. *Phys. Rev. B* **92**(11), 115118 (2015)
118. Sales, B.C.: Electron crystals and phonon glasses: a new path to improved thermoelectric materials. *MRS Bull.* **23**(1), 15–21 (1998)
119. Debye, P.: The theory of specific warmth. *Ann. Phys.* **39**(14), 789–839 (1912)
120. Dangic, D., Murphy, A.R., Murray, E.D., Fahy, S., Savic, I.: Coupling between acoustic and soft transverse optical phonons leads to negative thermal expansion of GeTe near the ferroelectric phase transition. *Phys. Rev. B* **97**(22), 224106 (2018)
121. Bocharov, D., Krack, M., Rafalskij, Y., Kuzmin, A., Purans, J.: Ab initio molecular dynamics simulations of negative thermal expansion in ScF_3 : the effect of the supercell size. *Comput. Mater. Sci.* **171**, 109198 (2020)
122. D'Ambrumeni, S., Zbiri, M., Chippindale, A.M., Hibble, S.J.: Phonon dynamics in the layered negative thermal expansion compounds $\text{Cu}_x\text{Ni}_{2-x}(\text{CN})_4$. *Phys. Rev. B* **100**(9), 094312 (2019)
123. Wendt, D., Bozin, E., Neufeind, J., Page, K., Ku, W., Wang, L.M., Fultz, B., Tkachenko, A.V., Zaliznyak, I.A.: Entropic elasticity and negative thermal expansion in a simple cubic crystal. *Sci. Adv.* **5**(11), 2748 (2019)
124. Peierls, R.E.: *Quantum Theory of Solids*. Oxford University Press, London (1955)
125. Ziman, J.M.: *Electrons and Phonons*. Oxford University Press, London (1960)
126. Callaway, J.: Model for lattice thermal conductivity at low temperatures. *Phys. Rev.* **113**(4), 1046–1051 (1959)
127. Klemens, P.G.: The thermal conductivity of dielectric solids at low temperatures—theoretical. *Proc. R. Soc. Lon. Ser. A* **208**(1092), 108–133 (1951)
128. Morelli, D.T., Slack, G.A.: High lattice thermal conductivity solids. In: Shindé, S.L., Goela, J.S. (eds.) *High Thermal Conductivity Materials*, pp. 37–68. Springer, New York (2006)
129. Slack, G.A.: Nonmetallic crystals with high thermal-conductivity. *J. Phys. Chem. Solids* **34**(2), 321–335 (1973)
130. Fugallo, G., Lazzeri, M., Paulatto, L., Mauri, F.: Ab initio variational approach for evaluating lattice thermal conductivity. *Phys. Rev. B* **88**(4), 045430 (2013)
131. Chernatynskiy, A., Phillpot, S.R.: Phonon transport simulator (PhonTS). *Comput. Phys. Commun.* **192**, 196–204 (2015)
132. Zhou, F., Nielson, W., Xia, Y., Ozolins, V.: Lattice anharmonicity and thermal conductivity from compressive sensing of first-principles calculations. *Phys. Rev. Lett.* **113**(18), 185501 (2014)
133. Kohn, W., Sham, L.J.: Self-consistent equations including exchange and correlation effects. *Phys. Rev.* **140**(4a), 1133–1138 (1965)
134. Tian, Z.T., Garg, J., Esfarjani, K., Shiga, T., Shiomi, J., Chen, G.: Phonon conduction in PbSe, PbTe, and $\text{PbTe}_{1-x}\text{Se}_x$ from first-principles calculations. *Phys. Rev. B* **85**(18), 184303 (2012)
135. Baroni, S., de Gironcoli, S., Dal Corso, A., Giannozzi, P.: Phonons and related crystal properties from density-functional perturbation theory. *Rev. Mod. Phys.* **73**(2), 515–562 (2001)
136. Li, W., Carrete, J., Katcho, N.A., Mingo, N.: ShengBTE: a solver of the Boltzmann transport equation for phonons. *Comput. Phys. Commun.* **185**(6), 1747–1758 (2014)
137. Togo, A., Chaput, L., Tanaka, I.: Distributions of phonon lifetimes in Brillouin zones. *Phys. Rev. B* **91**(9), 094306 (2015)
138. Carrete, J., Vermeersch, B., Katre, A., van Roekeghem, A., Wang, T., Madsen, G.K.H., Mingo, N.: almaBTE: a solver of the space-time dependent Boltzmann transport equation for phonons in structured materials. *Comput. Phys. Commun.* **220**, 351–362 (2017)
139. Assadi, M.H.N., Katayama-Yoshida, H.: Native point defects in Ti_3GeC_2 and Ti_2GeC . *Comput. Mater. Sci.* **128**, 103–108 (2017)
140. Savic, I., Mingo, N., Stewart, D.A.: Phonon transport in isotope-disordered carbon and boron-nitride nanotubes: is localization observable? *Phys. Rev. Lett.* **101**(16), 165502 (2008)
141. Katcho, N.A., Carrete, J., Li, W., Mingo, N.: Effect of nitrogen and vacancy defects on the thermal conductivity of diamond: an ab initio Green's function approach. *Phys. Rev. B* **90**(9), 094117 (2014)
142. Arrighoni, M., Carrete, J., Mingo, N., Madsen, G.K.H.: First-principles quantitative prediction of the lattice thermal conductivity in random semiconductor alloys: the role of force-constant disorder. *Phys. Rev. B* **98**(11), 115205 (2018)
143. Protik, N.H., Carrete, J., Katcho, N.A., Mingo, N., Broido, D.: Ab initio study of the effect of vacancies on the thermal conductivity of boron arsenide. *Phys. Rev. B* **94**(4), 045207 (2016)
144. Katre, A., Carrete, J., Dongre, B., Madsen, G.K.H., Mingo, N.: Exceptionally strong phonon scattering by B substitution in cubic SiC. *Phys. Rev. Lett.* **119**(7), 075902 (2017)

145. Murakami, T., Shiga, T., Hori, T., Esfarjani, K., Shiomi, J.: Importance of local force fields on lattice thermal conductivity reduction in $\text{PbTe}_{1-x}\text{Se}_x$ alloys. *EPL* **102**(4), 46002 (2013)
146. Puligheddu, M., Gygi, F., Galli, G.: First-principles simulations of heat transport. *Phys. Rev. Mater.* **1**(6), 060802 (2017)
147. Bouzid, A., Zaoui, H., Palla, P.L., Ori, G., Boero, M., Massobrio, C., Clerib, F., Lampin, E.: Thermal conductivity of glassy GeTe_4 by first-principles molecular dynamics. *Phys. Chem. Chem. Phys.* **19**(15), 9729–9732 (2017)
148. Snyder, G.J., Toberer, E.S.: Complex thermoelectric materials. *Nat. Mater.* **7**(2), 105–114 (2008)
149. Seko, A., Togo, A., Hayashi, H., Tsuda, K., Chaput, L., Tanaka, I.: Prediction of low-thermal-conductivity compounds with first-principles anharmonic lattice-dynamics calculations and Bayesian optimization. *Phys. Rev. Lett.* **115**(20), 205901 (2015)
150. Feng, T.L., Lindsay, L., Ruan, X.L.: Four-phonon scattering significantly reduces intrinsic thermal conductivity of solids. *Phys. Rev. B* **96**(16), 161201 (2017)
151. Xia, Y.: Revisiting lattice thermal transport in PbTe : the crucial role of quartic anharmonicity. *Appl. Phys. Lett.* **113**(7), 073901 (2018)
152. Ioffe, A.F., Regel, A.R.: *Progress in Semiconductors*, vol. 4. Wiley, New York (1960)
153. Allen, P.B., Feldman, J.L., Fabian, J., Wooten, F.: Diffusons, locons and propagons: character of atomic vibrations in amorphous Si. *Philos. Mag. B* **79**(11–12), 1715–1731 (1999)
154. Seyf, H.R., Yates, L., Bougher, T.L., Graham, S., Cola, B.A., Detchprohm, T., Ji, M.-H., Kim, J., Dupuis, R., Lv, W., Henry, A.: Rethinking phonons: the issue of disorder. *Npj Comput. Mater.* **3**(1), 49 (2017)
155. Trubitsin, V.Y., Dolgusheva, E.B.: Anharmonic effects and vibrational spectrum of bcc Zr under pressure studied by molecular dynamics simulations. *Phys. Rev. B* **76**(2), 024308 (2007)
156. Romero, A.H., Gross, E.K.U., Verstraete, M.J., Hellman, O.: Thermal conductivity in PbTe from first principles. *Phys. Rev. B* **91**(21), 214310 (2015)
157. Dewandre, A., Hellman, O., Bhattacharya, S., Romero, A.H., Madsen, G.K.H., Verstraete, M.J.: Two-step phase transition in SnSe and the origins of its high power factor from first principles. *Phys. Rev. Lett.* **117**(27), 276601 (2016)
158. Zhou, J.J., Hellman, O., Bernardi, M.: Electron-phonon scattering in the presence of soft modes and electron mobility in SrTiO_3 perovskite from first principles. *Phys. Rev. Lett.* **121**(22), 226603 (2018)
159. Aseginolaza, U., Bianco, R., Monacelli, L., Paulatto, L., Calandra, M., Mauri, F., Bergara, A., Errea, I.: Phonon collapse and second-order phase transition in thermoelectric SnSe . *Phys. Rev. Lett.* **122**(7), 075901 (2019)
160. Giustino, F., Cohen, M.L., Louie, S.G.: Electron-phonon interaction using Wannier functions. *Phys. Rev. B* **76**(16), 165108 (2007)
161. Noffsinger, J., Giustino, F., Malone, B.D., Park, C.H., Louie, S.G., Cohen, M.L.: EPW: a program for calculating the electron-phonon coupling using maximally localized Wannier functions. *Comput. Phys. Commun.* **181**(12), 2140–2148 (2010)
162. Cao, J., Querales-Flores, J.D., Murphy, A.R., Fahy, S., Savic, I.: Dominant electron-phonon scattering mechanisms in n-type PbTe from first principles. *Phys. Rev. B* **98**(20), 205202 (2018)
163. Liu, T.H., Zhou, J.W., Liao, B.L., Singh, D.J., Chen, G.: First-principles mode-by-mode analysis for electron-phonon scattering channels and mean free path spectra in GaAs . *Phys. Rev. B* **95**(7), 075206 (2017)
164. Cao, J., Querales-Flores, J.D., Fahy, S., Savic, I.: Thermally induced band gap increase and high thermoelectric figure of merit of n-type PbTe . *Mater. Today Phys.* **12**, 100172 (2019)
165. Guo, F., Liu, Z., Zhu, M.F., Zheng, Y.S.: Electron-phonon scattering limited hole mobility at room temperature in a MoS_2 monolayer: first-principles calculations. *Phys. Chem. Chem. Phys.* **21**(41), 22879–22887 (2019)
166. Chen, Y.N., Ma, J.L., Wen, S.H., Li, W.: Body-centered-cubic structure and weak anharmonic phonon scattering in tungsten. *Npj Comput. Mater.* **5**, 98 (2019)
167. Jain, A., McGaughey, A.J.H.: Thermal transport by phonons and electrons in aluminum, silver, and gold from first principles. *Phys. Rev. B* **93**(8), 081206 (2016)
168. Wang, Y., Lu, Z., Ruan, X.L.: First principles calculation of lattice thermal conductivity of metals considering phonon-phonon and phonon-electron scattering. *J. Appl. Phys.* **119**(22), 225109 (2016)
169. Lehmann, T., Ryndyk, D.A., Cuniberti, G.: Enhanced thermoelectric figure of merit in polycrystalline carbon nanostructures. *Phys. Rev. B* **92**(3), 035418 (2015)
170. Fei, R., Faghaninia, A., Soklaski, R., Yan, J.-A., Lo, C., Yang, L.: Enhanced thermoelectric efficiency via orthogonal electrical and thermal conductances in phosphorene. *Nano Lett.* **14**(11), 6393–6399 (2014)
171. Ramayya, E.B., Maurer, L.N., Davoody, A.H., Knezevic, I.: Thermoelectric properties of ultrathin silicon nanowires. *Phys. Rev. B* **86**(11), 115328 (2012)
172. Butler, K.T., Sai Gautam, G., Canepa, P.: Designing interfaces in energy materials applications with first-principles calculations. *Npj Comput. Mater.* **5**(1), 19 (2019)
173. Zahid, F., Lake, R.: Thermoelectric properties of Bi_2Te_3 atomic quintuple thin films. *Appl. Phys. Lett.* **97**(21), 212102 (2010)
174. Saha, B., Sands, T.D., Waghmare, U.V.: Thermoelectric properties of HfN/ScN metal/semiconductor superlattices: a first-principles study. *J. Phys. Condens. Matter* **24**(41), 415303 (2012)
175. Saha, B., Sands, T.D., Waghmare, U.V.: First-principles analysis of ZrN/ScN metal/semiconductor superlattices for thermoelectric energy conversion. *J. Appl. Phys.* **109**(8), 083717 (2011)
176. Xiong, K., Wang, W., Alshareef, H.N., Gupta, R.P., White, J.B., Gnade, B.E., Cho, K.: Electronic structures and stability of $\text{Ni/Bi}_2\text{Te}_3$ and $\text{Co/Bi}_2\text{Te}_3$ interfaces. *J. Phys. D* **43**(11), 115303 (2010)
177. Li, G., Hao, S., Aydemir, U., Wood, M., Goddard III, W.A., Zhai, P., Zhang, Q., Snyder, G.J.: Structure and failure mechanism of the thermoelectric $\text{CoSb}_3/\text{TiCoSb}$ interface. *ACS Appl. Mater. Interfaces* **8**(46), 31968–31977 (2016)
178. She, W., Liu, Q., Mei, H., Zhai, P., Li, J., Liu, L.: First-principles study on the tensile properties and failure mechanism of the CoSb_3/Ti interface. *J. Electron. Mater.* **47**(6), 3210–3217 (2018)
179. Li, G., An, Q., Li, W., Goddard, W.A., Zhai, P., Zhang, Q., Snyder, G.J.: Brittle failure mechanism in thermoelectric skutterudite CoSb_3 . *Chem. Mater.* **27**(18), 6329–6336 (2015)
180. Geisler, B., Blanca-Romero, A., Pentcheva, R.: Design of n- and p-type oxide thermoelectrics in $\text{LaNiO}_3/\text{SrTiO}_3(001)$ superlattices exploiting interface polarity. *Phys. Rev. B* **95**(12), 125301 (2017)
181. Ozdogan, K., Kahaly, M.U., Kumar, S.R.S., Alshareef, H.N., Schwingenschlögl, U.: Enhanced carrier density in Nb-doped SrTiO_3 thermoelectrics. *J. Appl. Phys.* **111**(5), 054313 (2012)
182. Baldereschi, A., Baroni, S., Resta, R.: Band offsets in lattice-matched heterojunctions: a model and first-principles calculations for GaAs/AlAs . *Phys. Rev. Lett.* **61**(6), 734 (1988)
183. Curtarolo, S., Setyawan, W., Wang, S., Xue, J., Yang, K., Taylor, R.H., Nelson, L.J., Hart, G.L., Sanvito, S., Buongiorno-Nardelli, M.: AFLOWLIB.ORG: a distributed materials properties repository from high-throughput ab initio calculations. *Comput. Mater. Sci.* **58**, 227–235 (2012)

184. Jain, A., Ong, S.P., Hautier, G., Chen, W., Richards, W.D., Dacek, S., Cholia, S., Gunter, D., Skinner, D., Ceder, G.: Commentary: the materials project: a materials genome approach to accelerating materials innovation. *APL Mater.* **1**(1), 011002 (2013)
185. Saal, J.E., Kirklin, S., Aykol, M., Meredig, B., Wolverton, C.: Materials design and discovery with high-throughput density functional theory: the open quantum materials database (OQMD). *Jom* **65**(11), 1501–1509 (2013)
186. Belsky, A., Hellenbrandt, M., Karen, V.L., Luksch, P.: New developments in the Inorganic Crystal Structure Database (ICSD): accessibility in support of materials research and design. *Acta Cryst. B* **58**(3), 364–369 (2002)
187. Downs, R.T., Hall-Wallace, M.: The American Mineralogist crystal structure database. *Am. Mineral.* **88**(1), 247–250 (2003)
188. Jain, A., Shin, Y., Persson, K.A.: Computational predictions of energy materials using density functional theory. *Nat. Rev. Mater.* **1**(1), 1–13 (2016)
189. Gorai, P., Stevanović, V., Toberer, E.S.: Computationally guided discovery of thermoelectric materials. *Nat. Rev. Mater.* **2**(9), 1–16 (2017)
190. Mathew, K., Singh, A.K., Gabriel, J.J., Choudhary, K., Sinnott, S.B., Davydov, A.V., Tavazza, F., Hennig, R.G.: MPInterfaces: a materials project based Python tool for high-throughput computational screening of interfacial systems. *Comput. Mater. Sci.* **122**, 183–190 (2016)
191. Mathew, K., Montoya, J.H., Faghaninia, A., Dwarakanath, S., Aykol, M., Tang, H., Chu, I.-H., Smidt, T., Bocklund, B., Horton, M.: Atomate: a high-level interface to generate, execute, and analyze computational materials science workflows. *Comput. Mater. Sci.* **139**, 140–152 (2017)
192. Miyata, M., Ozaki, T., Takeuchi, T., Nishino, S., Inukai, M., Koyano, M.: High-throughput screening of sulfide thermoelectric materials using electron transport calculations with OpenMX and BoltzTraP. *J. Electron. Mater.* **47**(6), 3254–3259 (2018)
193. Li, R., Li, X., Xi, L., Yang, J., Singh, D.J., Zhang, W.: High-throughput screening for advanced thermoelectric materials: diamond-like ABX₂ compounds. *ACS Appl. Mater. Interfaces* **11**(28), 24859–24866 (2019)
194. Faghaninia, A., Yu, G., Aydemir, U., Wood, M., Chen, W., Rignanes, G.-M., Snyder, G.J., Hautier, G., Jain, A.: A computational assessment of the electronic, thermoelectric, and defect properties of bournonite (CuPbSbS₃) and related substitutions. *Phys. Chem. Chem. Phys.* **19**(9), 6743–6756 (2017)
195. Chen, W., Pöhls, J.-H., Hautier, G., Broberg, D., Bajaj, S., Aydemir, U., Gibbs, Z.M., Zhu, H., Asta, M., Snyder, G.J.: Understanding thermoelectric properties from high-throughput calculations: trends, insights, and comparisons with experiment. *J. Mater. Chem. C* **4**(20), 4414–4426 (2016)
196. Park, J., Faghaninia, A., Jain, A., Ricci, F., Hautier, G., Frost, J.: AMSET: ab initio scattering and transport. <https://hackingmaterials.lbl.gov/amset/> (2020). Accessed 20 May 2020
197. Assadi, M.H.N., Katayama-Yoshida, H.: Restoration of long range order of Na ions in Na_xCoO₂ at high temperatures by sodium site doping. *Comput. Mater. Sci.* **109**, 308–311 (2015)
198. Assadi, M.H.N., Gutiérrez Moreno, J.J., Fronzi, M.: High-performance thermoelectric oxides based on spinel structure. *ACS Appl. Energy Mater.* **3**(6), 5666–5674 (2020)
199. Núñez-Valdez, M., Allahyari, Z., Fan, T., Oganov, A.R.: Efficient technique for computational design of thermoelectric materials. *Comput. Phys. Commun.* **222**, 152–157 (2018)

Publisher's Note Springer Nature remains neutral with regard to jurisdictional claims in published maps and institutional affiliations.